Quaternary Science Reviews 153 (2016) 97–121

Contents lists available at ScienceDirect

Quaternary Science Reviews

journal homepage: www.elsevier.com/locate/quascirev

The build-up, configuration, and dynamical sensitivity of the Eurasian ice-sheet complex to Late Weichselian climatic and oceanic forcing

Henry Patton [a, *], Alun Hubbard [a], Karin Andreassen [a], Monica Winsborrow [a], Arjen P. Stroeven [b, c]

[a] CAGE—Centre for Arctic Gas Hydrate, Environment and Climate, Department of Geology, UiT The Arctic University of Norway, 9037 Tromsø, Norway
[b] Geomorphology and Glaciology, Department of Physical Geography, Stockholm University, Stockholm, Sweden
[c] Bolin Centre for Climate Research, Stockholm University, Sweden

ARTICLE INFO

Article history:
Received 16 August 2016
Received in revised form
14 October 2016
Accepted 18 October 2016
Available online 30 October 2016

Keywords:
Ice-sheet modelling
Eurasian ice sheet complex
Late Weichselian
Palaeo ice-sheet reconstruction
Dynamic ice behaviour
Palaeo climate
Landscape evolution
Subglacial erosion
Barents Sea ice sheet
Fennoscandian ice sheet

ABSTRACT

The Eurasian ice-sheet complex (EISC) was the third largest ice mass during the Last Glacial Maximum (LGM), after the Antarctic and North American ice sheets. Despite its global significance, a comprehensive account of its evolution from independent nucleation centres to its maximum extent is conspicuously lacking. Here, a first-order, thermomechanical model, robustly constrained by empirical evidence, is used to investigate the dynamics of the EISC throughout its build-up to its maximum configuration. The ice flow model is coupled to a reference climate and applied at 10 km spatial resolution across a domain that includes the three main spreading centres of the Celtic, Fennoscandian and Barents Sea ice sheets. The model is forced with the NGRIP palaeo-isotope curve from 37 ka BP onwards and model skill is assessed against collated flowsets, marginal moraines, exposure ages and relative sea-level history. The evolution of the EISC to its LGM configuration was complex and asynchronous; the western, maritime margins of the Fennoscandian and Celtic ice sheets responded rapidly and advanced across their continental shelves by 29 ka BP, yet the maximum aerial extent (5.48×10^6 km^2) and volume (7.18×10^6 km^3) of the ice complex was attained some 6 ka later at c. 22.7 ka BP. This maximum stand was short-lived as the North Sea and Atlantic margins were already in retreat whilst eastern margins were still advancing up until c. 20 ka BP. High rates of basal erosion are modelled beneath ice streams and outlet glaciers draining the Celtic and Fennoscandian ice sheets with extensive preservation elsewhere due to frozen subglacial conditions, including much of the Barents and Kara seas. Here, and elsewhere across the Norwegian shelf and North Sea, high pressure subglacial conditions would have promoted localised gas hydrate formation.

1. Introduction

The Eurasian ice-sheet complex (EISC) at its maximum stand comprised an amalgam of three distinct and initially independent ice sheets – the marine-terminating ice sheet that covered the United Kingdom, Ireland and sectors of the North Sea (herein referred to as the Celtic Ice Sheet (CIS)), the mainly terrestrial-based Fennoscandian Ice Sheet (FIS), and the marine-based Barents (and Kara) Sea Ice Sheet (BSIS). Although each ice sheet was affected by unique and heterogeneous climatic and oceanographic boundary conditions (Marsiat and Valdes, 2001; Siegert and Marsiat, 2001), they converged to form a single, massive ice complex during peak conditions at the Last Glacial Maximum (LGM) (Bradwell et al., 2008; Winsborrow et al., 2010) (Fig. 1), with a volume almost treble that of the present-day Greenland Ice Sheet (Hughes et al., 2016). Progress in reconstructing the extent, volume, and timing of Weichselian glaciation across northern Eurasia using ice sheet and Earth rheology models (e.g., Bowen et al., 2002; Forsström and Greve, 2004; Peltier, 2004; Siegert and Dowdeswell, 2004) has traditionally suffered from geological constraints being limited to terrestrial sectors of the former ice complex (e.g., Kleman et al., 1997; Boulton et al., 2001; Svendsen et al., 2004). However, advances in the last decade have vastly improved the resolution and quality of geophysical data across marine sectors, which has vastly improved understanding of the processes, chronology, and drivers of the EISC during the Late Weichselian (e.g., Ottesen et al., 2005;

* Corresponding author.
E-mail address: henry.patton@uit.no (H. Patton).

http://dx.doi.org/10.1016/j.quascirev.2016.10.009

Andreassen et al., 2007; Jessen et al., 2010; Clark et al., 2012; Bjarnadóttir et al., 2014; Patton et al., 2015; Hughes et al., 2016).

In this study, we combine and utilise these integrated datasets to constrain a numerical model of the last EISC as it advanced from its independent nucleation centres to its maximum configuration. From this optimum experiment, we explore the sensitivity and probable uncertainties in our reconstruction by examining the effects on ice build-up from a range of climate, mass balance and ice flow parameters. We then direct these primary modelling results to help elucidate and resolve a number of key empirical debates surrounding the maximum EISC, including:

- What were the principal drivers and critical timings associated with the asynchronous development of the initially independent ice centres? Through direct comparison with LGM-stage flowsets and proximity tracking of modelled ice-margin positions, the asymmetric evolution of the complex is examined in detail.
- How thick were the main centres of ice dispersal? Ice-surface profiles are compared against exposure age transects from across the domain, and the pattern of isostatic loading at the LGM is also explored.
- What impact did the ice complex have on the landscape during the LGM? A time-integrated map of potential erosion is determined from model output that differentiates, in detail, zones of permanently cold-based ice from areas susceptible to glacial abrasion.

2. The northern Eurasian palaeo-environmental record

2.1. Palaeoclimate

Whilst the timing of ice sheet inception during the transition between marine oxygen isotope stage (MIS) 3/2 in northern Eurasia remains poorly resolved, a growing body of evidence indicates that Britain, Fennoscandia, and terrestrial areas in the Barents Sea hosted only limited remnants of the former Mid-Weichselian ice sheet during MIS 3 (>c. 33 ka BP) (e.g., Andreassen et al., 1985; Whittington and Hall, 2002; Arnold et al., 2002; Bos et al., 2004; Brown et al., 2007; Ukkonen et al., 2007; Mangerud et al., 2008a,b; Alexanderson et al., 2010; Wohlfarth and Näslund, 2010; Helmens and Engels, 2010; Mangerud et al., 2010; Möller et al., 2013).

Global ice-sheet maxima during the last glacial cycle attained an apex during a diachronous period from 33 to 19 ka BP, centred around 26.5 ka BP (Peltier and Fairbanks, 2006; Clark et al., 2009). For the three sub-domains of the ice-sheet complex, this climate deterioration during the LGM had a widespread but variable impact. The CIS, the western-most and smallest centre of nucleation, was dominated by a relatively warm and maritime climate fed by a weakened but still active North Atlantic current. As such, its growth and decay was rapid and dynamic, expanding and shrinking in response to fluctuations in climate and sea-level (Hubbard et al., 2009; Scourse et al., 2009; Clark et al., 2012). The topographic relief that dominates the western seaboard of Scandinavia drove eastward terrestrial-based ice advance and ultimately an extensive ice sheet (Kleman and Stroeven, 1997; Boulton et al., 2001; Svendsen et al., 2004; Kleman et al., 2008; Stroeven et al., 2016). Conversely, the BSIS was almost entirely marine-based, grounded in water depths of up to 550 m (Polyak et al., 1997), thus a direct analogue to the present-day West Antarctic Ice Sheet. Palaeoclimate proxies, such as limited glacier growth across Russian sectors (Mangerud et al., 2008a,b; Barr and Clark, 2011; Möller et al., 2015), as well as ice modelling studies (Siegert and Dowdeswell, 2004; van den Berg, van de Wal and Oerlemans, 2008; Clason et al., 2014) reveal that the general climate of eastern Eurasia was hyper-arid, reflecting precipitation starvation due to the rain-shadow effect of an expanded FIS further west.

2.2. LGM configuration

The evolution and dimensions of the maximum Late Weichselian ice extent are reasonably well established in most sectors of Eurasia, with continued progress in absolute dating narrowing the temporal uncertainties (Bradwell et al., 2008; Hughes et al., 2011; Clark et al., 2012; Hughes et al., 2016; Stroeven et al., 2016) (Fig. 1). For much of the western margin of the ice complex, glacial extension to the continental shelf break is recorded by an established geomorphological footprint (e.g., Ottesen et al., 2005; Clark et al., 2012) and associated deposition of glacigenic sediments onto the trough-mouth fans at the terminus of ice streams (Laberg and Vorren, 1995; Vorren and Laberg, 1997; Sejrup et al., 2005). The positioning of ice-rafted debris within dated cores indicate a relatively early advance to the shelf occurred in these sectors between c. 27-24 cal ka BP (Sejrup et al., 2000; Scourse et al., 2009; Dunlop et al., 2010; Jessen et al., 2010). To the south and east, sedimentological and glacial landform mapping (e.g., Kleman et al., 1997; Svendsen et al., 2004; Kjær et al., 2006; Stroeven et al., 2016) coupled with new cosmogenic sampling and radiometric dating (Svendsen et al., 2015; Cuzzone et al., 2016; Hughes et al., 2016; Stroeven et al., 2016) has provided tight constraints on the terrestrial limits across much of continental Europe, with peak extent reached between 25 and 17 ka BP. However, the accuracy of cosmogenic nuclide exposure dating within peripherally glaciated areas remains contentious (Heyman et al., 2011; Briner et al., 2016; Stroeven et al., 2016).

In contrast, the extent and configuration of ice across the Kara Sea is the least certain of the entire complex, limited by a lack of data. Dated tectonic push moraines on the northern Taimyr Peninsula (Alexanderson et al., 2002) and the distribution of till across the northern Kara Sea (Polyak et al., 2008) indicate that grounded ice is likely to have reached the northern Taimyr Peninsula ca. 20 ka BP. The drivers and dynamics of this postulated advance in relation to those of the EISC remains equivocal and essentially unresolved.

The chronology and configuration of CIS-FIS coalescence over the North Sea is also largely undetermined (Clark et al., 2012; Hughes et al., 2016), though the timing of confluent shelf-edge glaciation is thought to have occurred sometime between 29 and 25 ka BP (Bradwell et al., 2008; Sejrup et al., 2009), with subsequent separation occurring around 18.5 ka BP (Sejrup et al., 2016). The timing of FIS and BSIS convergence is similarly poorly documented; based on the youngest ages of shell fragments incorporated within till and glacially reworked sediments in central Bjørnøyrenna, convergence here probably occurred sometime after c. 26 ka BP (Hald et al., 1990; Elverhøi et al., 1993).

3. The model

The 3D thermomechanical ice sheet model applied is a first-order approximation of the Stokes-equations adopted from Blatter (1995) by Hubbard (1999, 2000) and is an approach that has been independently used by Marshall et al. (2005) to model the Laurentide ice sheet, Pollard and DeConto (2007) for the Antarctic ice sheet, and most recently by Morlighem et al. (2016) to model the evolution of a major Greenland outlet glacier. It has previously been applied to Iceland (Hubbard, 2006), the British Isles (Golledge et al., 2009; Hubbard et al., 2009; Kuchar et al., 2012; Patton et al., 2013) and Patagonia (Hubbard et al., 2005) to investigate the build-

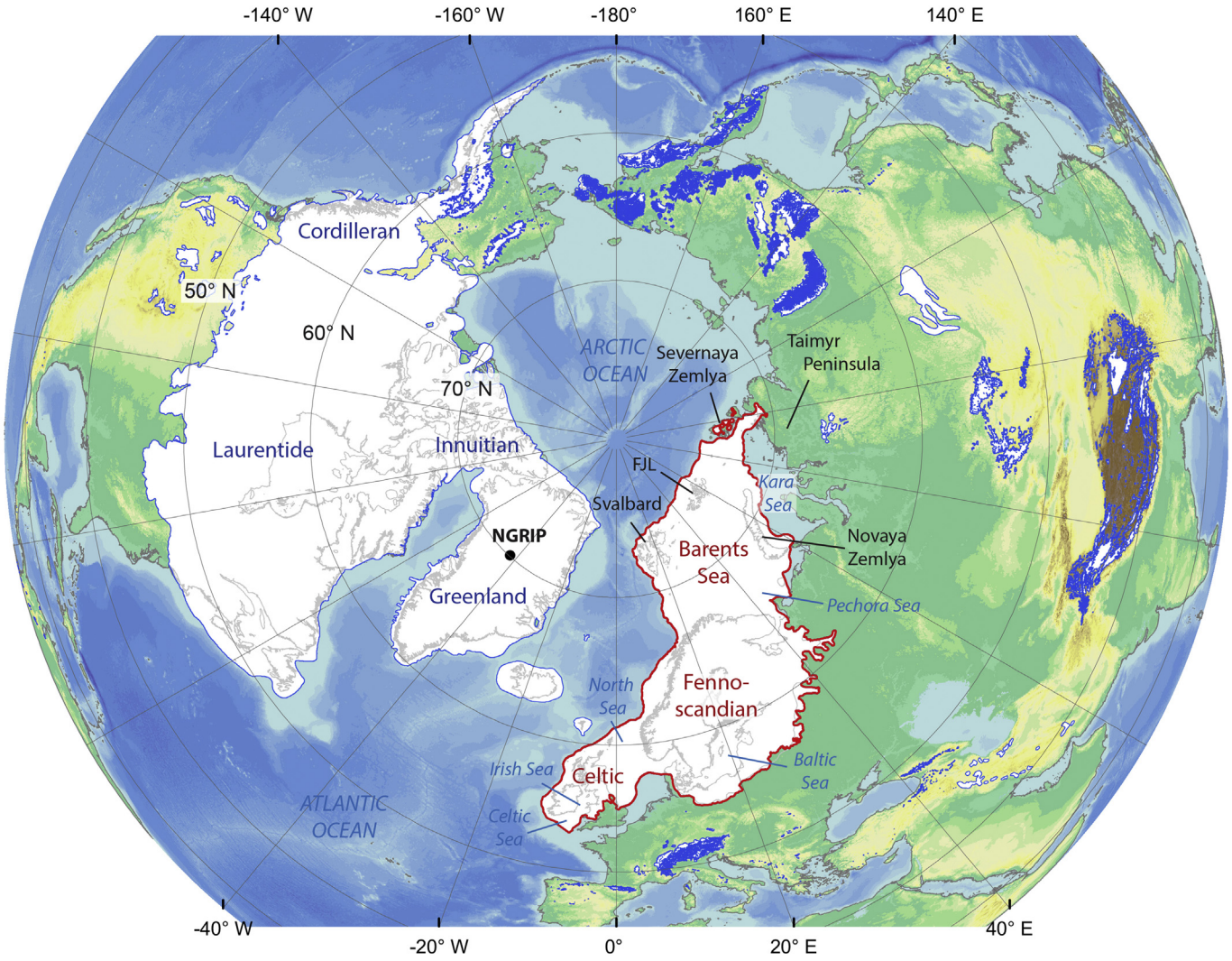

Fig. 1. The Late Weichselian Eurasian Ice Sheet Complex (EISC; red outline) in the context of Northern Hemispheric glaciation. The EISC comprised three semi-independent ice-sheets, though maximum extension in all sectors was not contemporaneous. Acronyms used: FJL (Franz Josef Land), NGRIP (North Greenland Ice Core Project). Glacial limits compiled from Ehlers and Gibbard (2007), Patton et al. (2015) and Stroeven et al. (2016). Topography: The GEBCO_2014 Grid, www.gebco.net. (For interpretation of the references to colour in this figure legend, the reader is referred to the web version of this article.)

up, extent and deglaciation of the LGM ice sheets that occupied these regions. The approach adopted to solve the stress/strain field equates to the L1L2 classification of higher-order models defined by Hindmarsh (2004), and includes longitudinal (membrane) stresses. Including higher order stresses becomes increasingly important over steep terrain and/or under conditions of low basal traction. The model performs well in the ISMIP-HOM benchmark experiments when compared to second-order and full-Stokes schemes (Pattyn et al., 2008) and has been applied and validated against observations of 3D ice flow at Haut Glacier d'Arolla (Hubbard et al., 1998) and Glacier de Tsanfluron (Hubbard et al., 2003; Chandler et al., 2006) under complex ice rheologies.

Boundary conditions include: i) a present-day reference climate comprising monthly mean air temperature and precipitation, ii) basal topography, and iii) the geothermal heat flux. The model is integrated forward in time on a finite-difference grid with a resolution of 10 km through perturbations in temperature and eustatic sea-level. Gridded input and output is projected under an equal area Lambert Azimuthal projection, with a central meridian of 73°E. Common model parameters, constants, and values are presented in Table 1. Model construction, assumptions and limitations are fully described in the references above; detailed description here is limited to where its implementation is specifically different from previous applications.

3.1. Surface mass balance

The mass balance of a glacier is determined as the difference between gains (accumulation) and losses (ablation), usually over one year. In simple terms, these net changes are dominated by precipitation and melting across the ice surface, and through the loss of icebergs at marine-terminating margins. In the model, surface mass balance is determined by a positive degree-day (PDD) scheme applied according to Laumann and Reeh (1993), and derives total melt from integrated monthly positive temperatures. Monthly temperature is calculated from the mean annual air temperature (MAAT) data, assuming a sinusoidal function with maximum and minimum peaks equating to mean monthly July and January temperatures. Cumulative PDDs for each month are calculated using a probability function based on a relationship between the standard deviation of daily to mean monthly temperature. Despite the limitations of such schemes (van der Veen,

2002; Golledge et al., 2010; Seguinot, 2013), their general ability to simulate glacier responses in contemporary Arctic environments (Braithwaite, 1995; Jóhannesson et al., 1995; De Woul and Hock, 2005) lends confidence in their use. Palaeo-climate forcing is implemented from the NGRIP $\delta^{18}O$ record (Andersen et al., 2004), that is linearly scaled between a maximum prescribed temperature depression and present-day conditions. Bulk precipitation is distributed evenly throughout the year and accumulates as snow when the surface temperature falls below a threshold of 1 °C. Winter expansion of sea ice across the North Atlantic probably impacted upon precipitation seasonality during stadial conditions, leading to a summer bias in the annual precipitation distribution across maritime sectors (Thomas et al., 2008; Koenigk et al., 2009). Annual precipitation totals were thus likely greater than implied by the effective precipitation volumes recorded by glacier geometries here due to the increased losses from the system associated with summer rainfall (Golledge et al., 2010).

Spatial and temporal patterns of temperature and precipitation are dynamically coupled with the evolving ice sheet through applied temperature/precipitation – elevation (lapse-rate) relationships. These are derived from multiple-regression of meteorological data from the WorldClim database (Hijmans et al., 2005; Version 1.4) during the climatic reference period 1950 to 2000 (Fig. 2A–C; Table 2). To account for the broad-scale variability between maritime conditions across western Europe and the continental climate of eastern Europe and northern Russia (Fig. 2A–C), the modelled climate is calculated across three prescribed sub-domains (Fig. 2D). Their extents are determined by the probable maximum extent and influence of each ice sheet, with a broad overlap given to avoid sharp climatic contrasts. Where transitions occur between sub domains, changes in climate parameters such as MAAT suppression and bulk precipitation are calculated assuming a linear gradient. Primary climate differences between these sub domains for our optimum reconstruction are given in Table 4, with general trends including a northwards decrease in temperature cooling and northwards increase in precipitation availability.

A limitation of the model is that we do not calculate the general circulation. Large-scale changes in climate related to shifts in atmospheric circulation are thus not accounted for, although broad scale distributions, for example rain shadow effects, can be incorporated manually by the application of linear gradients.

Independent variables used in regression analysis to determine the spatial distribution of temperature include easting, northing, latitude, longitude, elevation, and (maritime) proximity to the North Atlantic thermohaline circulation (Fig. 2E). To determine the spatial pattern of the precipitation, an additional independent parameter - δ_{temp} - was used as a measure for continentality, being the residual between the summer and winter temperatures (Fig. 2F). R^2 values are typically >90% for temperature across all three climatic domains, indicating temperature distributions can be readily parameterised within the model. Precipitation for CIS and FIS sectors yield weaker correlations for the present-day distribution with a R^2 value of c. 60%, though the BSIS sector is better described with an R^2 value of 86% (Table 2).

Sublimation is also incorporated into mass balance calculations in the High Arctic. Net water vapour fluxes to and from the ice sheet surface are important components of ablation in cold continental settings where humidity is low (e.g., Fujii and Kusunoki, 1982; Kameda et al., 1997; Box et al., 2004). A modelling study over the Greenland ice sheet revealed that these components can account for up to 12.5% (74 km^3 a^{-1}) net reduction in accumulation from snowfall (Ohmura et al., 1999). Field based studies provide confirmation of these model results with sublimation accounting for a 12–23% total precipitation loss (Box and Steffen, 2001). Across the Greenland ice sheet, sublimation is controlled by two factors – latitude, which is a proxy for the length and intensity of direct solar radiation, and elevation, since high-elevation sites generally have stronger temperature inversions and lower surface winds as katabatic winds tend to accelerate towards the coast as the surface slope angle increases. Sublimation is calculated based on a multiple regression analysis of these two *in situ* measurements (Table 3) from the Greenland Climate Network (GC-Net) (One level method: Box and Steffen, 2001). In the absence of more certain contributions of blowing snow sublimation rates on temporal and spatial trends of the surface mass balance (e.g., Déry and Yau, 2002), and for simplicity, calculated sublimation fluxes are applied evenly throughout the year.

3.2. Topography

Topographic and bathymetric datasets were melded from the International Bathymetric Chart of the Arctic Ocean (IBCAO) dataset (Jakobsson et al., 2012) above 60°N, and GEBCO_14 (http://www.gebco.net/) for areas south of 60°N. All topographic data were merged onto a custom Lambert Azimuthal equal-area projection and resampled to 10 km horizontal resolution using a nearest neighbour algorithm. Isostatic loading is implemented using an elastic lithosphere/relaxed asthenosphere scheme described by Le Meur and Huybrechts (1996) which provides a computationally pragmatic solution in the absence of a full spherical earth model.

3.3. Calving and basal dynamics

Calving losses at marine terminating margins are coupled to changing sea level (Waelbroeck et al., 2002) using a standard empirical function relating the calving flux (U_c) to ice thickness (H) and water depth, W_d (Brown et al., 1982; van der Veen, 1999). The sensitivity of calving to, for example, variations in ocean temperature (Luckman et al., 2015) can be controlled spatially and temporally through a variable calving coefficient A_c (Hubbard, 2006) (Table 1):

$$U_c = A_C H W_d.$$

Basal sliding is determined by a Weertman (1964) sliding law, adjusted using an exponential decay function to initiate basal motion at sub pressure-melting temperatures (e.g., Fowler, 1986; Kleman et al., 1999; Wilch and Hughes, 2000). The sliding rate factor for temperatures, $\theta, \leq 0.75$ K below the pressure-melting point A_s, is defined by:

$$A_s = A_s^0 \exp[-\gamma\theta_m - \theta],$$

where A_s^0 is the sliding rate factor at the pressure-melting point temperature, θ_m, and the coefficient γ is set to 1 K^{-1} (Hindmarsh and Le Meur, 2001). At 0.75 K below the pressure-melting point, sliding is 0.47 of its value at the pressure-melting point.

A spatially-variable distribution of geothermal heat flux is applied, interpolated onto the model domain from core measurements sourced from the Global Heat Flow Data Base (Pollack et al., 1993). While geothermal heat flux is largely dominated by low mean continental shield values close to 50 mW m^{-2} throughout Eurasia, several hotspots exist offshore of northern Finnmark, Norway, and eastern Svalbard (Fig. 2G).

3.4. Implementation and assumptions

All the numerical experiments are hot-started from an initial modelled ice configuration at 37.23 ka BP, a period of relatively warm interglacial climate conditions concurrent with minimal

Table 1
Principal parameters, constants and values used to force the ice-sheet model.

Parameter		Value	Units
g	Gravity	9.81	m s^{-2}
ρ	Density of ice	910	kg m^{-3}
ρ_w	Density of sea water	1028	kg m^{-3}
N	Glen flow-law exponent	3	
A_{weert}	Weertman sliding parameter	7.5×10^{-14}	
γ	Sub-melt sliding coefficient	1	K
m	Sliding-law exponent	1–3	
SF	Sliding factor	2.5	
A_s	Sliding-law coefficient	1.8×10^{-5}	m kPa^{-3} a^{-1}
A_0	Deformation enhancement	50	
a	Material constant		
	$T^* < 263.15$	1.14×10^{-5}	Pa^{-3} a^{-1}
	$T^* \geq 263.15$	5.47×10^{10}	Pa^{-3} a^{-1}
Q	Creep activation energy		
	$T^* < 263.15$	60×10^3	J mol^{-1}
	$T^* \geq 263.15$	139×10^3	J mol^{-1}
A_c	Calving parameter	1.07–29.4	a^{-1}
DDF	Degree day factor	0.005	mm $°C^{-1}$ d^{-1}
T	Temperature	–	K
T^*	(pressure melt corrected)	$T - 8.7 \times 10^{-4}H$	K
$T_{snow\text{-}rain}$	Snow-rain threshold	1.0	°C
R	Universal gas constant	8.314	J mol^{-1} K^{-1}
k_i	Thermal conductivity	$2115.3 + 7.93\ (T–273.15)$	J m^{-1} K^{-1} a^{-1}
C_p	Specific heat capacity	$3.1 \times 10^8 \exp(-0.0057T)$	J kg^{-1} K^{-1} a^{-1}
φ	Internal frictional heating	–	J m^{-3} a^{-1}
G	Geothermal heat flux	15–705	mW m^{-2}
D	Flexural rigidity	5.0×10^{20}	N m
δt	Time step	0.0034	a
δx_i	Finite difference interval	1×10^4	m
	Central meridian	73	°E
	Latitude of origin	90	°N
x_{min}	Domain dimensions	−4,750,000	Lambert azimuthal equal area
x_{max}		1,600,000	(central meridian 73°E)
y_{min}		−3,000,000	
y_{max}		−190,000	

terrestrial-based ice cover (Fig. 2H). Ice extent, thickness and the loaded topography are determined from a Mid-Weichselian (MIS 4) experiment with sufficient spin-up time for the ice sheet and isostatic loading to attain a transient equilibrium with the forcing climate. As there are sparse observations to constrain glacial limits during the MIS 3/2 transition, the extent of inherited ice beyond our assumed and modelled restricted limits represents a major unknown (Wohlfarth and Näslund, 2010; Helmens, 2014; Patton et al., 2015). A radiocarbon date on terrestrial plant macrofossils (34.7 ka BP) in southern Norway supports ice-free conditions extending to the heart of the FIS domain during this time (Paus et al., 2011). Radiocarbon dating of woolly rhinoceros bones indicate that western central Scotland was also ice-free c. 35 ka BP (Jacobi et al., 2009), with IRD records off western Scotland confirming that the CIS was sufficiently active to generate icebergs during MIS 3 (Hibbert et al., 2010). The extent of amino acid racemization on mollusc shells has also been used to infer reduced (less than present-day) ice cover over Novaya Zemlya (Mangerud et al., 2008b). In summary, the restricted ice sheet configuration used to hot-start the numerical experiments from 37.23 ka BP onwards corresponds with the limited empirical evidence available that indicates a minimum glaciated time-slice (cf. section 2.1). Furthermore, it also broadly matches the reconstruction of a slender mountain-centred Fennoscandian ice sheet by Hughes et al. (2016) for this period.

4. Optimal reconstruction

Perturbation of model parameters and forcing essentially yields an indefinite number of ice-sheet configurations ranging from the highly plausible to the completely improbable. However, through systematic parameter tuning, validated against empirical evidence (e.g., Svendsen et al., 2004; Hughes et al., 2016), a controlled iteration procedure enables model refinement towards a 'best-fit' scenario. Figs. 3C and 4 depicts the optimal simulation for Eurasia – an experiment that has good correspondence with dated ice limits and a strong level of coherence with available geophysical evidence (Larsen et al., 1999; Winsborrow et al., 2010; Clark et al., 2012). This optimal parameter set is described in Table 4.

While the optimal reconstruction honours broad geological constraints across much of the domain, local regions could be better-resolved using fine-tuned boundary conditions and forcing (for example, increased basal motion in a warmer and wetter localised climate). However, given the scale of uncertainties and numerical limitations associated with model formulation, inputs, boundary conditions, parameterisation, and the available empirical constraints, *ad hoc* amendments to achieve meso-scale improvements are not pursued. As it is presented, the model represents an internally consistent solution to the ice flow equations which yields output that is valid from the continental to regional scale potentially down to tens of kilometres – the operational resolution of the model. Limitations and uncertainties in boundary conditions, past oceanic and climatic conditions, a multitude of processes and parameterisations - many of which are sub-grid or simply ignored in the model – preclude sensible attempts at interpretation and comparison of model output on the local scale. The temporal evolution of the optimal reconstruction through to the LGM is described below:

4.1. 37–30 ka BP

With the onset of climate deterioration from 37 ka BP, all ice-cap

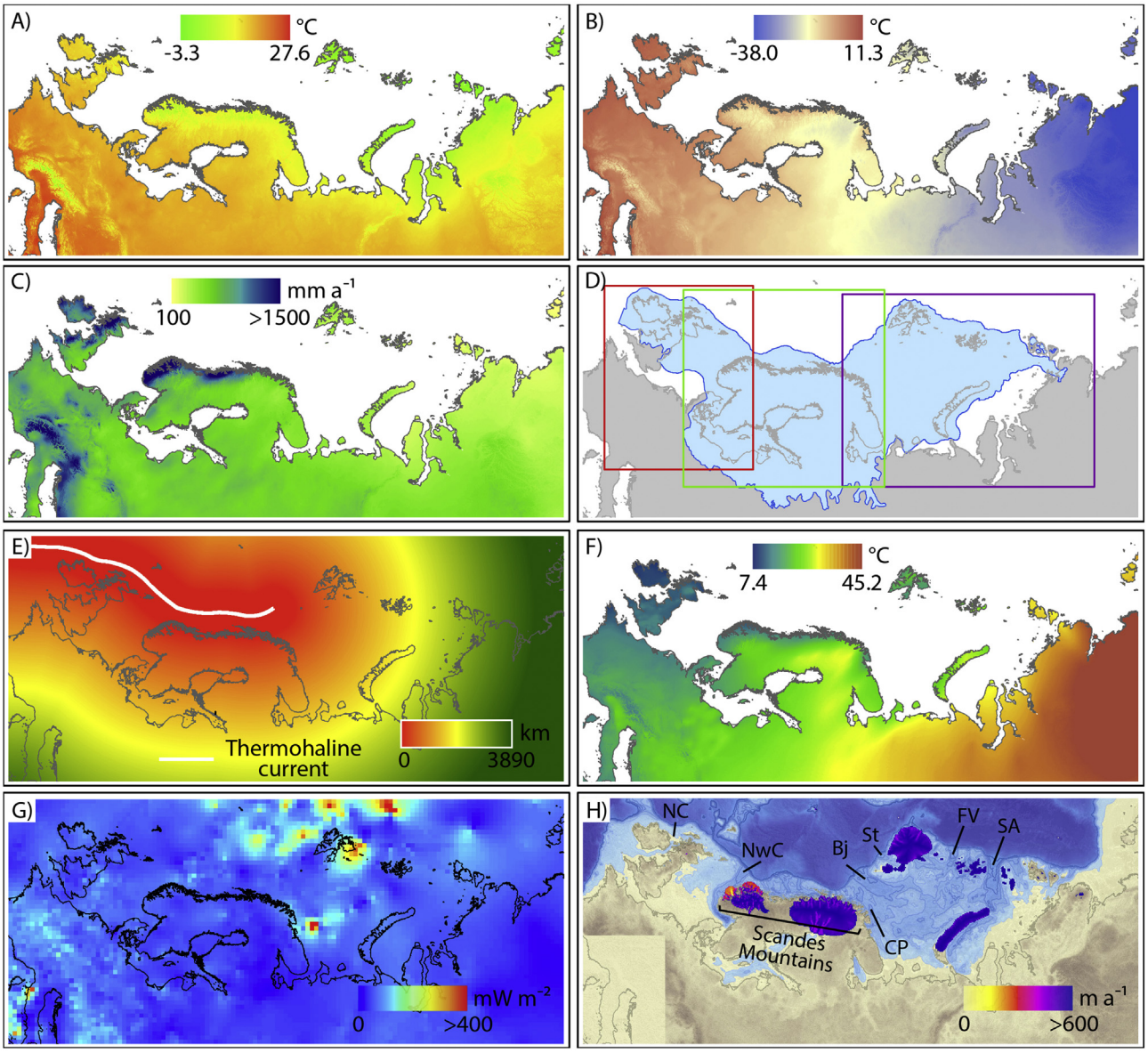

Fig. 2. Boundary conditions employed. A) Mean summer air temperature (July); B) Mean winter air temperature (January); C) Mean annual precipitation; D) Maximum extension of the LGM ice-sheet complex (blue), and limits of the independently calibrated climatic regimes (Table 2); E) Proximity to the North Atlantic thermohaline circulation (modified from Straneo et al., 2012); F) δ_{temp} – difference between winter and summer air temperatures, and proxy for continentality; G) Geothermal heat flux (gridded from Pollack et al., 1993); and H) Initial isostatically-adjusted topography, sea level, and ice extent at MIS 3 (37.23 ka BP) inherited from an MIS4 experiment and used to kickstart LGM experiments. Trough acronyms: Bj – Bjørnøyrenna; CP – Coast Parallel; FV – Franz Victoria; NC – North Channel; NwC – Norwegian Channel; SA – Saint Anna Trough; St – Storfjordrenna . Meteorological data were sourced from the WorldClim database (Hijmans et al., 2005; Version 1.4) during the climatic reference period 1950–2000. (For interpretation of the references to colour in this figure legend, the reader is referred to the web version of this article.)

remnants of the Mid Weichselian glaciation switch to a state of accumulation and positive mass balance. Glaciers and ice caps build-up to cover much of the Scottish Highlands, and the two major nucleation centres over southern Norway and northern Scandinavia expand sufficiently to merge north of Trondheim. Across the Barents Sea, rapid regrowth of ice in the Svalbard archipelago means the ice margin quickly assumes a position at the shelf break to the west and north. Elsewhere, isolated, cold-based ice caps occupy Franz Josef Land, Novaya Zemlya and other sub-aerially exposed banks.

By 30 ka BP most ice caps throughout the domain are sufficiently large and dynamic for fast flowing outlet glaciers to be active (Fig. 4A). For the CIS, the Moray Firth and Loch Linne offer the largest ice flow pathways over Scotland. In Fennoscandia, the first incursions into the Norwegian Channel and the Skagerrak occur with ice also flowing southwards into large proglacial lakes filling the Baltic Sea basin. At this time ice over Svalbard, Franz Josef Land and Storfjordbanken is merged, with Storfjorden now occupied by fast-flowing ice to the shelf break.

4.2. 30–27 ka BP

Further, climatic deterioration drives rapid expansion and thickening of the CIS and FIS, with fast-flowing ice streams attaining the western shelf break by c. 29 ka BP (Fig. 4B). Scottish based ice is now sufficiently large that it merges with independent ice caps over Ireland, and extends into the North Sea as far as the Orkney Islands. In Fennoscandia, the Baltic Sea ice stream

Table 2
Parameters and R^2 values from multiple-regression analyses of climate across the model domain, detailing the ability of the model to reproduce present-day climate patterns utilising relatively few parameters. Eastings, northings and proximities are regressed in Lambert Azimuthal projection units (m), latitudes and longitudes in decimal degrees, and elevations in m a.s.l.

	Parameter	Celtic	Fenno-scandia	Barents Sea
Dependent:	**Summer temperature**			
Independent:	Easting	−4.699E-5	−2.233E-5	3.093E-5
	Northing	2.37E-5	−7.497E-5	4.946E-5
	Latitude	*N/A*	*N/A*	−15.74
	Longitude	3.967	*N/A*	−0.5979
	Elevation	−4.766E-2	−5.179E-2	−3.692E-2
	Proximity	*N/A*	−4.843E-5	*N/A*
	Intercept	10.75	3.578	1359
R^2 value		89.43%	89.67%	92.93%
Dependent:	**Winter temperature**			
Independent:	Easting	−7.211E-5	−5.575E-5	−2.382E-5
	Northing	*N/A*	8.791E-5	*N/A*
	Latitude	2.184	*N/A*	−2.004
	Longitude	*N/A*	*N/A*	−1.398
	Elevation	−5.781E-2	−4.911E-2	−4.924E-2
	Proximity	−2.296E-5	7.19E-5	−2.088E-5
	Intercept	−348	−102.2	44.49
R^2 value		92.2%	81.58%	96.0%
Dependent:	**Mean temperature**			
Independent:	Easting	−2.197E-5	−5.401E-6	−1.365E-5
	Northing	*N/A*	*N/A*	2.601E-5
	Latitude	−1.766	−5.823	−8.692
	Longitude	*N/A*	*N/A*	−0.8701
	Elevation	−5.294E-2	−4.994E-2	−4.098E-2
	Proximity	*N/A*	−2.166E-5	*N/A*
	Intercept	103.4	404.9	644.4
R^2 value		93.85%	93.85%	92.93%
Dependent:	**Annual precipitation**			
Independent:	Easting	6.6E-4	2.291E-3	1.521E-5
	Northing	−1.2E-3	*N/A*	8.751E-5
	Latitude	−58.94	−266.6	−31.07
	Longitude	−46.8	−37.92	−3.035
	Elevation	0.4682	0.1614	0.1076
	δtemp	−7.153	−3.926	−0.3889
	Proximity	−9.323E-4	−1.037E-3	9.847E-5
	Intercept	6717	2.528E4	2887
R^2 value		61.94%	60.17%	86.29%

Table 3
Parameters and the R^2 value from a multiple-regression analysis of sublimation across the Greenland ice sheet. Climate data sourced from Box and Steffen (2001).

	Parameter	Greenland
Dependent:	**Box1LM**	
Independent:	Latitude	3.279
	Elevation	0.05465
	Intercept	−400.3
Adjusted R^2 value (%):		86.13

dominates the outflow of the FIS, extending as far south as Latvia, balanced to the west by numerous and narrow outlet glaciers draining the Norwegian fjords. Other notable fast flow features include proto versions of the Irish Sea ice stream and the Norwegian Channel ice stream. Continued growth of the BSIS yields ice beginning to extend into the deeper troughs of Bjørnøyrenna and the Saint Anna Trough.

4.3. 27–23 ka BP

Temperature fluctuations during this timeframe lead to significant advances and retreats across southern sectors of the ice complex. However, in the Arctic, where fluctuations in MAAT do not rise above 0 °C, ice sheet growth continues. By c. 26 ka BP, ice occupies much of the Arctic Ocean margin, also merging with the Novaya Zemlya ice cap (Fig. 4C). Continued thickening of ice here also leads to the first signs of fast flow within Bjørnøyrenna, contemporaneous with outlet glaciers extending rapidly through the White Sea and out of northern Finnmark from the FIS.

At 24.5 ka BP the grounded BSIS fully converges with FIS, eventually forming an ice divide running northwards over Finnmark and the central banks of the Barents Sea (Fig. 4D). In response, the central dome of the BSIS gradually shifts to the south-east forcing ice advance into the Pechora Sea. Elsewhere, fast flowing outlet glaciers and lobes continue to expand margins across all sectors, with the Baltic Sea ice stream encroaching on continental Europe and CIS continuing to dominate the North and Irish seas.

4.4. 23–19 ka BP

By 23 ka BP, ice flowing through the Norwegian Channel expands the southwestern margin of FIS sufficiently to converge fully with CIS ice flowing into the North Sea (Fig. 4E). This coalescence quickly forms an east-west ice divide between Scotland and Norway, abruptly halting flow of the Norwegian Channel ice stream towards the shelf break.

At 22.7 ka BP, the EISC has its greatest areal extent and volume of 5.48×10^6 km^2 and 7.18×10^6 km^3, respectively (Fig. 3C), although not all LGM limits are attained synchronously at this time. Northwest Russia is the last sector to glaciate across the entire ice-sheet complex, being furthest away from the dominant moisture sources, the main ice nucleation centres and any notable ice streams. Ice flowing through the White Sea merges with Barents Sea ice flowing east along the Kola Peninsula and through the Pechora Sea to attain its maximum limit on the Kanin Peninsula c. 20.2 ka BP (Fig. 4F–G). A simultaneous surge of ice into the Dvina Basin marks the most eastern extent of modelled ice flow into northern Russia.

Ice expansion eastwards after 22.7 ka BP is marked by a general retreat of marine-terminating glaciers off the shelf break to less extensive, stable positions on the continental shelf, first in the Celtic and Norwegian seas, followed by the Barents Sea c. 1 ka later. After 20 ka BP, climate amelioration across the domain forces widespread ice sheet retreat across the majority of terrestrial and marine-based margins (Fig. 4H).

5. Model sensitivity

Using the optimal reconstruction described above as a reference scenario, further experiments were initiated to explore the sensitivity of the ice complex to a range of climate, mass balance and ice flow parameters. Such experiments reveal the sensitivity of the modelled ice complex to both internal and external forcing and helps identify the main uncertainties in the optimal reconstruction. A summary of the area, volume and ice thickness variations can be found in Fig. 3D–E and Table 5.

5.1. Sublimation sensitivity

Sublimation provides a significant sink for ice mass in cold-climate regimes, particularly where MAATs are consistently below freezing. In Antarctica it has been estimated that the processes of surface and blowing snow sublimation dispose about 17–20% of its annual precipitation (Déry and Yau, 2002), comparable to observations from Greenland weather stations (Box and Steffen, 2001). The effects of including water vapour fluxes within the model's mass balance budget are thus considerable, with an overall trend for a reduced ice extent and volume in all sectors, particularly across the High Arctic (Figs. 5 and 6A). At high elevation summits of

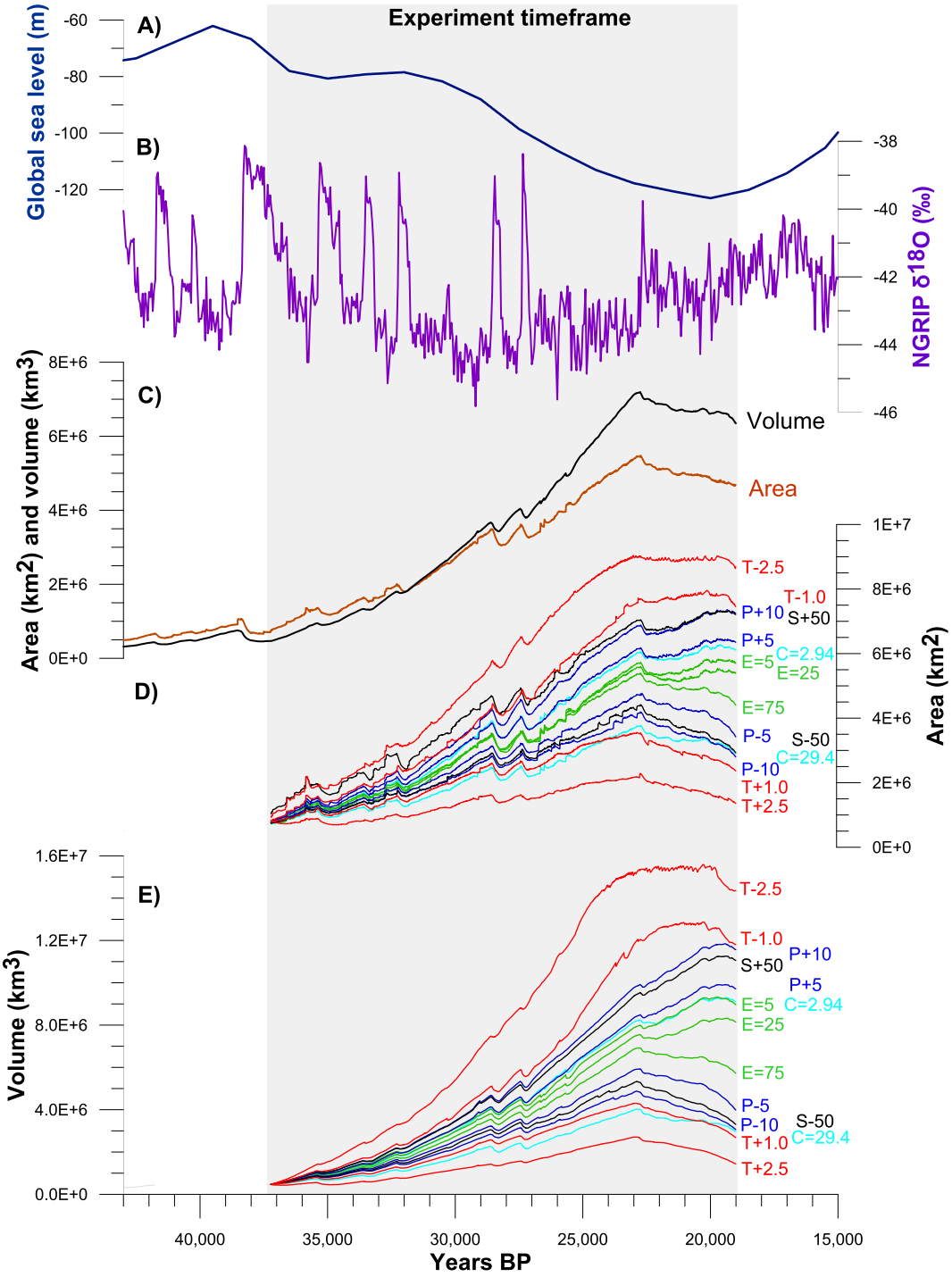

Fig. 3. The sea level (A; Waelbroeck et al., 2002) and NGRIP (B; Andersen et al., 2004) climate forcing curves used to drive LGM experiments, alongside the volumetric and areal evolution of the optimal EISC experiment (C; Fig. 4) and sensitivity experiments (D–E). All experiments are hot-started from an initial modelled ice configuration at 37.23 ka BP until 19.0 ka BP, with conditions inherited from a MIS 4 experiment allowing for sufficient spin-up time of the ice system and isostatic loading to attain a transient equilibrium with the forcing climate. Abbreviations used: T – temperature (°C); P – precipitation (%); S – sublimation (%); E – flow enhancement factor; C – calving sensitivity.

Fennoscandia, the reverse situation is true, with net condensation leading to ice accumulation.

Sensitivity to bulk changes in moisture fluxes are moderate relative to other climate parameter changes. Although all sectors experience deviations from the optimum extent, the most significant changes occur across high-latitude regions. Here, suppression of sublimation losses leads to widespread glaciation across the Kara Sea and Taimyr Peninsula (Fig. 6A). Under a scenario of enhanced sublimation, precipitation losses become greater still, leading to severely reduced volumes of each ice sheet centre such that all three centres become separated from each other.

5.2. Mean annual air temperature

Temperature forcing is, by far, the single-most important parameter within the ensemble of experiments (Figs. 3D–E, 6B).

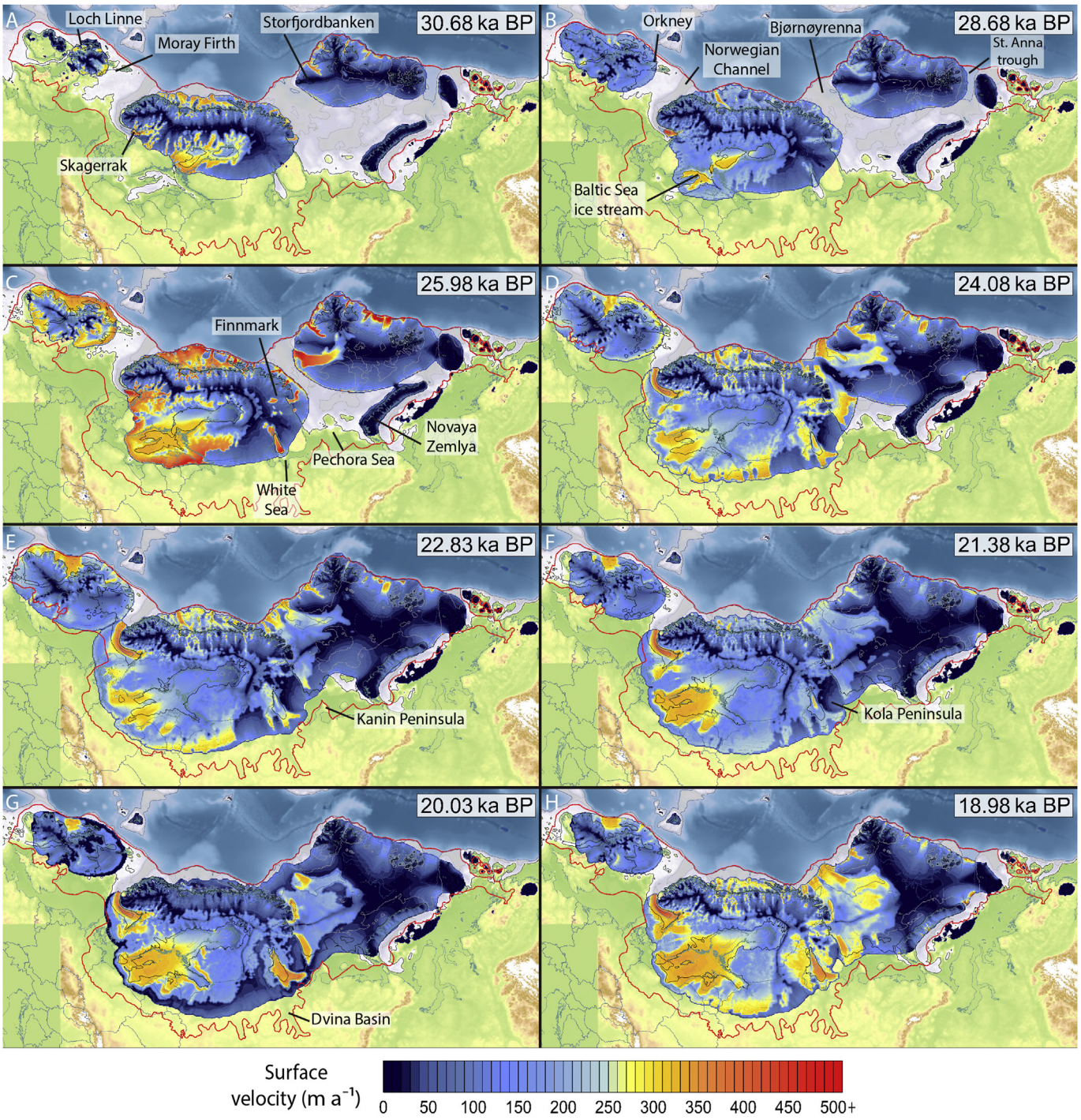

Fig. 4. Timeslices showing ice-surface velocities during build-up of the EISC from MIS 3 through to the LGM and initiation of deglaciation. Sea level is determined from the global sea-level forcing curve (Fig. 3A) and modelled isostatic loading effects. Red line indicates empirically derived maximum limits of glaciation. (For interpretation of the references to colour in this figure legend, the reader is referred to the web version of this article.)

With enhanced climate deterioration, the greatest changes occur across terrestrial sectors south of ~70°N, whereby reduction of MAATs drive increases in effective annual precipitation, leading to an expansive invasion of the continental European lowlands. As surface temperatures across the Barents Sea are already permanently below 0 °C in the optimum experiment, changes in ice volume due to increased snowfall input here are negligible, experiencing only a slight thickening related to enhanced buttressing from the FIS (Table 4).

High amplitude warming impacts on all sectors of the ice-sheet complex, resulting in enhanced surface ablation and severely restricted ice sheet limits. With a bulk rise of just 1 °C the CIS is restricted to the Scottish Highlands at the LGM, and disappears almost entirely under a 2.5 °C rise. Model sensitivity to warming lessens at northern latitudes, although the southern Barents Sea remains ice free under both scenarios at the LGM.

With fluctuations of only ±1 °C leading to considerable differences in ice sheet evolution, it follows that only a narrow envelope

Table 4
Model parameter values used in the optimal reconstruction of the EISC across the three climate sub-domains (Fig. 2D). Bulk precipitation percentages are proportional to the predicted present-day totals (cf. Table 2). The range of total effective annual precipitation values (i.e., the proportion of snowfall annually) is calculated from minimum and maximum MAATs between 37 and 19 ka BP at a central position within each climate sub domain and at 500 m a.s.l.

Parameter	Celtic	Fennoscandia	Barents
Temp. multiplier	−9.0 °C	−8.8 °C	−7.0 °C
Temp. offset	−3.65 °C	−2.9 °C	−1.3 °C
Bulk precipitation	67%	79.5%	100%
Annual effective precipitation	60-100%	71-100%	100%
Calving sensitivity (A_c)	26.5	14.7	5.9[a]

[a] 1.1 for latitudes above 78°N.

is plausible for correct parameterisation of the palaeo-climate. The dramatic differences of the CIS on the southern periphery of the complex during climatic cooling further indicates that this maritime region responded rapidly to climate change during the Late Weichselian. This contrasts with the BSIS, which is relatively insensitive to climate cooling beyond parameter values used in the optimum experiment. The distribution of ice across High Arctic sectors is, however, more susceptible and sensitive to variations in precipitation.

5.3. Precipitation distribution

The distribution of precipitation in the optimum experiment is perturbed from the present day distribution through imposed west-east and north-south gradients (Fig. 7). The majority of these fall into the category of rain-shadow gradients, with major reductions (between 60 and 75%) imposed in the lee of the ice divides of each semi-independent ice sheet (North Sea, continental Europe and the Kara Sea). A positive gradient is also required across Ireland (25%), enhancing orographic rainfall and thereby promoting the growth of independent ice caps in this warm maritime region. However, by far the largest modification is the positive gradient northwards across the Barents Sea (130%). This enhancement is justified on the basis of the large positive mass balance required for ice caps over Svalbard and Franz Josef Land to expand, merge and eventually coalesce with Fennoscandian ice. While this adjustment is closely associated with the imposed insensitivity to calving losses in this region (section 5.5), the lack of empirical data to constrain the extent of perennial sea ice or ice shelves during build-up from MIS 3 leaves the question of what controlled ice-sheet initiation in this sector open-ended.

Imposing a bulk 10% reduction in precipitation demonstrates the apparent importance of Barents Sea precipitation gradients, and results in an ice sheet with insufficient mass to coalesce with its Fennoscandian counterpart at the LGM (Fig. 6C). In other sectors, reduced mass input has a major impact leading to major reductions in terrestrial and marine-based ice extents, including permanent ice-free conditions in the North Sea. Similar to temperature reductions, increases in total precipitation lead to significantly greater changes in ice-complex geometry than reductions, the major factor being the ability to expand terrestrial-based margins far into continental Europe (Fig. 6C). However, the Barents Sea ice sheet being limited by the continental shelf break on two sides and a severe precipitation gradient eastwards, instead thickens significantly by up to 500 m compared to the optimum experiment.

5.4. Ice viscosity (A_0)

A conventional adaption of Glen's flow law within shallow-ice approximation based ice sheet models is the inclusion of an empirical flow enhancement (aka softening) coefficient, used to encompass the effects of crystal anisotropy and impurities on bulk ice deformation (Cuffey and Paterson, 2010). The most significant result of modifying strain rates is that softer ice tends to flow faster, resulting in a lower aspect ratio ice sheet and long-profiles of glaciers, while stiffer ice produces thicker glaciers and ice sheets with steeper profiles. Values applied typically range from 3 to 6 (Huybrechts and Oerlemans, 1990; Payne, 1999; Golledge et al., 2012), though values up to 80 have been used to model a low-aspect ratio Laurentide ice sheet (Tarasov and Peltier, 2000). Our optimum reconstruction uses a flow enhancement coefficient of 50. In terms of areal extent, sensitivity experiments for this parameter show the least magnitude variation (Fig. 6D). Stiffer ice (low A_0 values) leads to more expansive margins across terrestrial limits in Europe, associated with thicker, high-profile ice over Fennoscandia. However, the converse is true for marine limits in the Pechora and Kara seas. Here, thick (>500 m above the optimum experiment) ice leads to increased suppression of the bed and thus increased susceptibility to calving losses.

For experiments with "softer" ice (high A_0 values), outlet glaciers drawdown greater mass from the ice sheet interior to the margins. However, the resulting low aspect-ratio surface and hence thinner ice sheet exposes greater surface areas to surface melting processes, leading to more restrictive margins across terrestrial sectors. With $A_0 > 50$, perennial nunataks exist within the coastal region of southern Norway.

Table 5
Sensitivity analysis results of the optimum LGM experiment. Geometry values are taken from a consistent timeslice at 22.7 ka BP.

Parameter	Area ($\times 10^6$ km^2)	Δ area (%)	Volume ($\times 10^6$ km^3)	Δ volume (%)	Mean thickness (m)	Δ thickness (%)
Optimal experiment	**5.477**		**7.177**		**1310**	
Calving = 2.94	6.061	10.65	8.233	14.71	1358	3.67
Calving = 29.4	3.776	−31.05	4.002	−44.24	1060	−19.13
Flow enhancement = 5	5.727	4.56	7.984	11.24	1394	6.39
Flow enhancement = 25	5.601	2.27	7.540	5.06	1346	2.73
Flow enhancement = 75	5.390	−1.58	6.909	−3.73	1282	−2.18
Precipitation +5%	6.176	12.76	8.472	18.05	1372	4.69
Precipitation +10%	6.881	25.63	9.901	37.95	1439	9.81
Precipitation −5%	4.746	−13.36	5.918	−17.54	1247	−4.83
Precipitation −10%	4.195	−23.41	4.814	−32.93	1194	−12.43
Sublimation +50%	4.419	−19.32	5.275	−26.51	1194	−8.91
Sublimation −50%	7.050	28.71	9.522	32.67	1351	3.08
Temperature + 1 °C	3.539	−35.39	4.250	−40.78	1201	−8.34
Temperature +2.5 °C	2.285	−58.28	2.628	−63.39	1150	−12.24
Temperature −1 °C	7.683	40.26	12.044	67.82	1568	19.65
Temperature −2.5 °C	9.014	64.57	15.357	113.98	1704	30.02

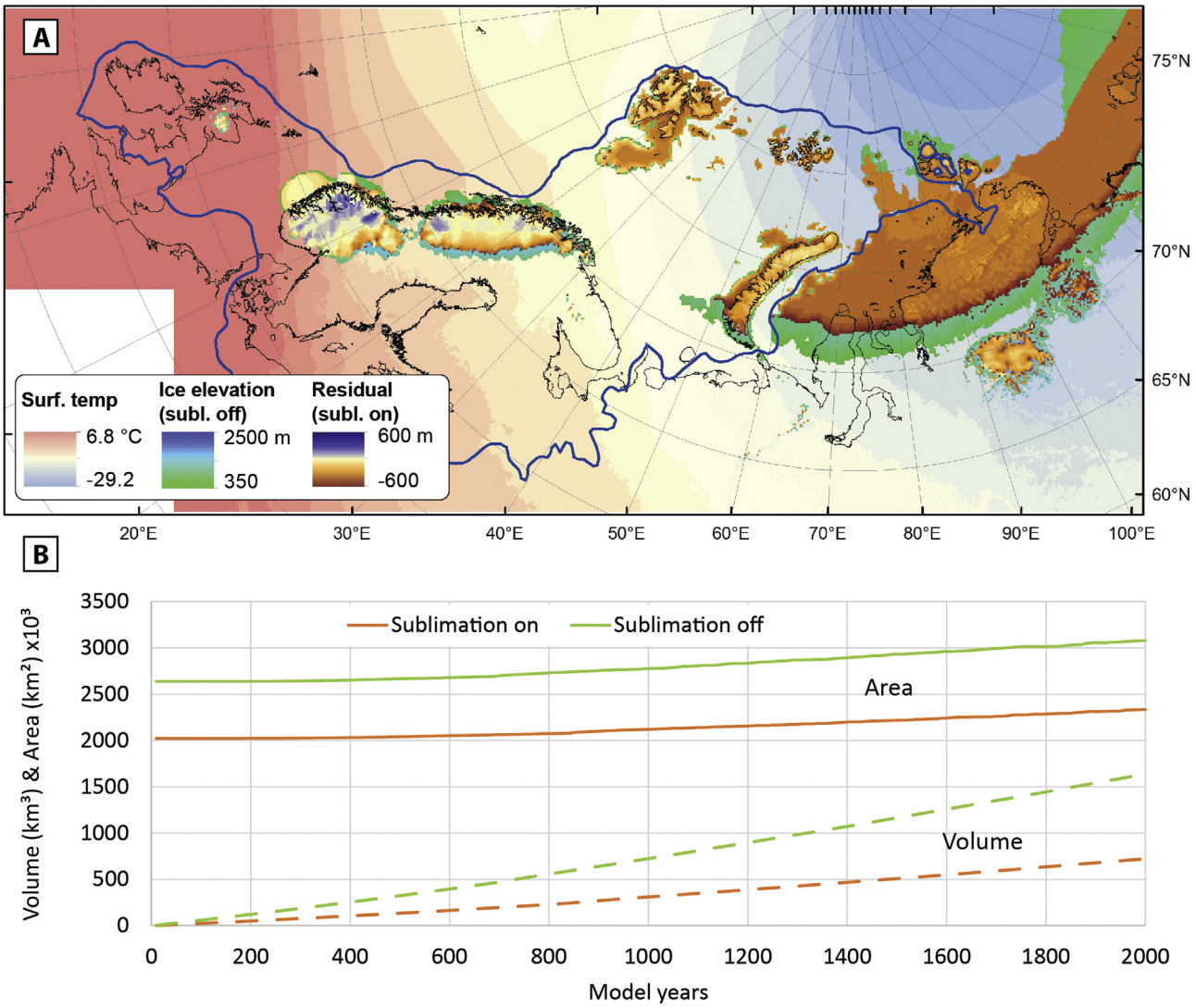

Fig. 5. The effects of modelled sublimation processes on ice-sheet evolution over the first 2000 years of model simulation with modern MAATs suppressed by 8 °C and a present-day precipitation distribution. (A) Surface elevation and extent of the ice complex with sublimation switched on (extent of the residual layer) and off. (B) Area-volume curves over 2000 model years, indicating a slower rate of growth of the ice sheet with sublimation processes included.

5.5. *Calving sensitivity (A_c)*

While ice shelves and floating ice are not explicitly accounted for in the ice-sheet model, their effects on margin stability can be partially resolved through spatial and temporal variations on the sensitivity of the calving parameter. Mass losses through calving can vary significantly via external drivers, including ocean temperature (Luckman et al., 2015), surface melting/hydrofracture (van der Veen, 1998), and the buttressing effects provided by sea ice, ice shelves or ice mélange (Joughin et al., 2008; Amundson et al., 2010; Todd and Christoffersen, 2014). In our optimum experiment, the calving flux is tuned separately for each ice sheet, broadly defined by a decrease in sensitivity northwards. For example, to facilitate growth of the marine-based BSIS, a significant reduction in the calving sensitivity parameter is required for ice to expand across the Barents Sea, up to a magnitude less than in regions further south (Table 4). This choice becomes apparent in the sensitivity experiment where $A_c = 29.4$ as growth of ice becomes severely limited to just sub-aerially exposed areas (Fig. 6E). Conversely, with a reduction in calving rates to $A_c = 2.94$, mass losses are reduced across the southern Barents Sea, leading to a thicker ice sheet at the LGM by c. 300 m. Further south, reduced calving leads to a persistence of ice across the North Sea through to 19 ka BP, as well as a slight expansion onto deeper banks west of Ireland and around the Faroe Islands.

6. Discussion

6.1. *Climatic and oceanographic forcing*

The expanse of the EISC domain creates a significant challenge for the purpose of modelling ice-sheet growth, chiefly due to wide response of climate patterns associated with climate deterioration and changes in ocean circulation. The partitioning of the model domain into three distinct climatic and oceanographic regimes with respect to each of the major ice sheet centres thus provides a useful approach into exploring the climatic and oceanographic differences that forced asymmetric growth of the EISC towards its maximum extent. Here we discuss insights garnered from the model experiments for each semi-independent ice sheet in relation

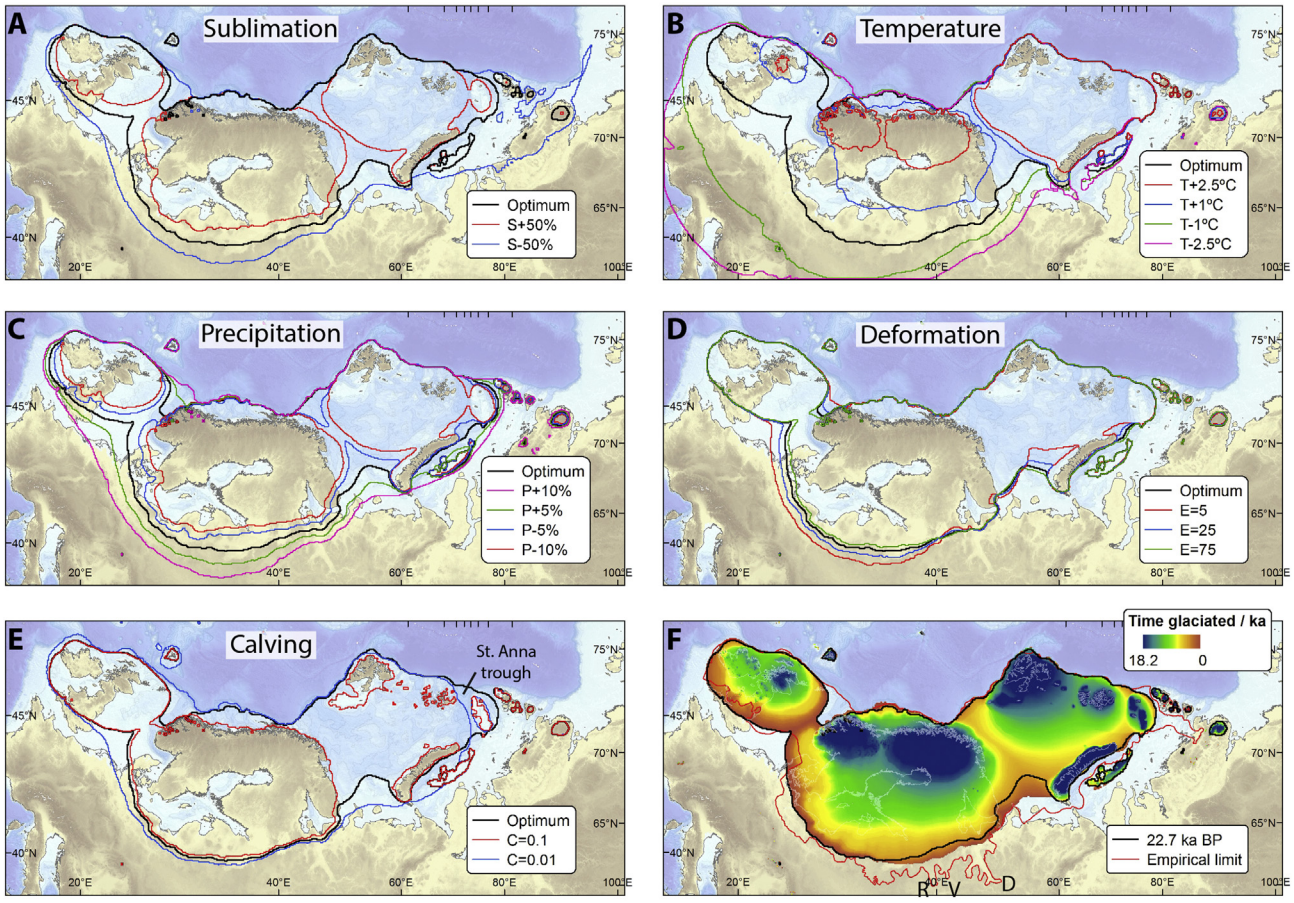

Fig. 6. A-E) Modelled glacial extents at 22.7 ka BP from sensitivity experiments for, respectively, sublimation, mean annual air temperature, annual precipitation, deformation enhancement, and calving sensitivity, compared with the same timeslice from the optimum experiment (black line); F) Maximum extension, and time glaciated, of the optimum modelled EISC between 37 and 19 ka BP compared with 22.7 ka BP and current empirical limits. Acronyms used: D – Dvina Basin; R – Rybinsk Basin; V – Vologda Basin.

to empirical observations.

6.1.1. *Barents Sea*

The expansion and merging of nucleation centres across vast marine sectors of the High Arctic is controlled by two principle factors. The first is a strongly modified precipitation distribution compared to that of the present-day (Figs. 2C and 7). In particular, the strong enhancement of bulk precipitation over the north-western Barents Sea by up to 130%, alongside a steep gradient loss eastwards down to levels of 34% of present-day values over the Kara Sea. This general decline in bulk precipitation eastwards is a common feature of previous modelling efforts in this region (Siegert et al., 2001; van den Berg, van de Wal and Oerlemans, 2008; Clason et al., 2014), and is supported by empirical insights from glacial extents across the Russian Arctic (Mangerud et al., 2008a,b; Fredin et al., 2012; Möller et al., 2015). Previous ice sheet and climate modelling have further implied that ice growth along the western Barents Sea was driven by a maritime climate that produced relatively high rates of precipitation (e.g., Hubberten et al., 2004). Relatively warm waters advected into the Norwegian Sea as far north as Spitsbergen between 27 and 22.5 ka BP, resulting in seasonally ice-free waters (Müller and Stein, 2014), therefore providing a crucial moisture source during this initial build-up of ice (Hebbeln et al., 1994; Knies et al., 1998). Although the magnitude of this gradient may be overly optimistic, it is possible that it could be weakened through more refined tuning of the distribution of sublimation losses (Fig. 6A).

The second factor necessary for the expansion of grounded Barents Sea ice is the strong reduction in the sensitivity to calving losses, particularly above 78°N (Table 4). Sensitivity experiments reveal that such suppression of calving is necessary to drive the expansion of grounded ice across deep marine sectors, especially the Saint Anna Trough in the far northeast (Fig. 6E). Radiocarbon dates from deglacial sediments lying above glacial diamicton indicate that this 550 m deep trough was fully glaciated during the Late Weichselian (Polyak et al., 1997). The application of reduced calving sensitivity across the High Arctic can be justified for several reasons. First, the presence of perennial sea ice across the Arctic Ocean between 30 and 17 ka BP north of the Fram Strait (Müller et al., 2009) would have provided a definite buttressing effect on outlet glaciers flowing towards the Arctic Ocean. Present-day observations from Jakobshavn Isbræ in Greenland show that variations in sea ice cover and ice mélange strength can lead to an effective cessation of frontal ablation rates, forcing significant seasonal terminus oscillations (Amundson et al., 2010). Secondly, calving rates of tidewater glaciers vary strongly with sub-surface ocean temperature (Luckman et al., 2015). While such temperatures are still underdetermined during the Late Weichselian, marine-terminating glaciers in sectors further south (and in closer proximity to subsurface warm Atlantic Water masses) were probably more prone to sub-marine melting (e.g., Bauch et al., 2001).

The lack of well-constrained limits on the eastern margin of the BSIS in the Kara Sea (cf. Hughes et al., 2016) makes this region particularly difficult to resolve with any confidence. In particular

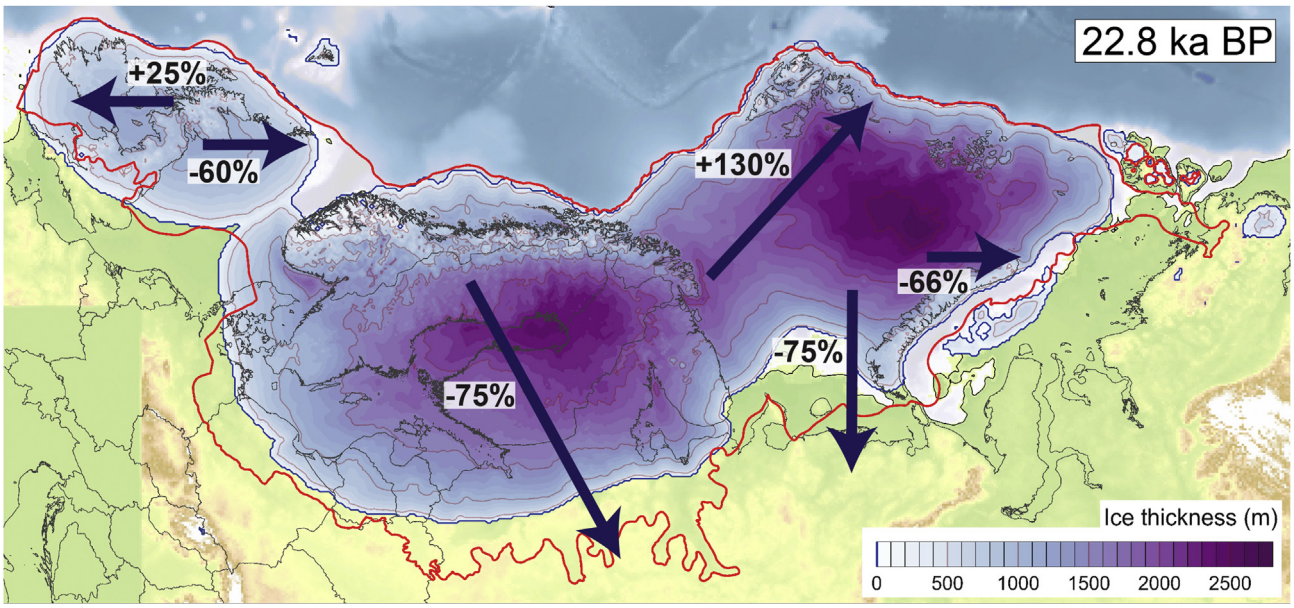

Fig. 7. Major modifications to the modern day precipitation distribution during the build-up of the Late Weichselian EISC.

the corridor of ice that is presumed to have flowed onto the Taimyr Peninsula as one coherent ice mass (Alexanderson et al., 2002; Polyak et al., 2002; Svendsen et al., 2004) appears glaciologically improbable, especially so when taking into consideration the presumed minimalist-style ice cover across Severnaya Zemlya (Möller et al., 2015) and lack of a southern connection of ice onto the peninsula in the Kara Sea (Stein et al., 2002; Spielhagen et al., 2004) (Fig. 1). Precipitation rates of <100 mm a^{-1} are required to limit the growth of the Severnaya Zemlya ice caps to within present-day limits (factoring in sublimation; present-day rates range between 150 and 250 mm a^{-1}), which in turn limits growth of ice on nearby shallow bank areas. It is therefore hypothesised that any growth of ice in this corridor during the Late Weichselian was marginal, with localised ice caps on sub-aerially exposed banks connected by ice shelves/perennial sea ice.

6.1.2. Fennoscandia

The high elevation topography and maritime climate of Norway together induce a relatively rapid expansion of the FIS to the Norwegian continental shelf break c. 29 ka BP. This, however, contradicts radiocarbon dated cave bones (Mangerud et al., 2010) and marine core evidence (Rørvik et al., 2010), which together indicate ice still remained onshore at this stage, with expansion into the Norwegian Sea occurring no earlier than c. 27.6 ka BP. One possible explanation for this discrepancy is the overestimation of the remnant ice cover during MIS 3 (Fig. 2H), and/or potentially more arid climate conditions during this interglacial restricting ice growth.

Disregarding some episodic perturbations, fast-flowing marine outlet glaciers continue to efficiently drain ice to the Norwegian Sea shelf break until c. 23 ka BP (#5 in Fig. 8A). After a rapid transition, a stable position is reached halfway between the shelf and present coastline for the next 4 ka. Oceanographic drivers do not appear to be responsible for this retreat phase, but rather widespread ice piracy associated with a long-term migration of the central ice divide eastwards through the Late Weichselian (Fig. 9). Widespread chronological dating has established an asynchronous configuration of maximum glaciation across Scandinavia (e.g., Larsen et al., 1999; Stroeven et al., 2016), depicted also in our model results here. The exacerbation of dry continental conditions across mainland Europe, due to the rain-shadow effect imposed by the ice sheet itself, appears critical for maintaining consistency with terrestrial limits east and south of FIS (Fig. 6C). An exception is the extension of ice lobes into the Dvina, Vologda, and Rybinsk basins in NW Russia, several hundred kilometres beyond the surrounding ice margin (Fig. 6F) (Stroeven et al., 2016). Here, Larsen et al. (2014) argued that the overstretching of the outlet glaciers into these basins was ice-dynamical rather than climatically driven, aided by ice flow over waterlain lacustrine sediments and tills with low shear strength, and supported by the dating of these advances late c. 17–16 ka BP.

The apparent ease and rapidity by which ice masses can develop over Fennoscandia (<5 ka – Fig. 4) has produced a palimpsest landscape characterised by contrasting geomorphological units, ranging from intact preglacial surface remnants and glacial landforms preserved beneath frozen beds through to deep glacial troughs scoured by the repeated occupation by ice streams (Kleman, 1994; Kleman and Stroeven, 1997). In this respect, the wet maritime climate experienced over western and northern Scandinavia is critical, driving the rapid development of initial cold-based ice caps over central mountain regions (Fig. 2C), progressing through to the maintenance of persistent and topographically confined ice streams under extensive ice-sheet glaciation (e.g., the Baltic, Norwegian Channel, and west Norwegian fjords) (Fig. 4).

6.1.3. Britain and Ireland

The wet, maritime conditions prevalent over northern Britain and western Fennoscandia meant that ice centres here responded rapidly to climate deterioration. Ice subsequently attained the westerly shelf breaks early by 29 ka BP (Fig. 8A), corroborating observations of pronounced IRD fluxes from western Scotland and Ireland at this time (Scourse et al., 2009). The sensitivity of this region to temperature and precipitation fluctuations (Fig. 6B–C) supports the contention that this ice sheet was highly dynamic, and led to a complex geomorphological palimpsest with multiple advance and retreat cycles (Greenwood and Clark, 2009; Clark et al., 2012; Hughes et al., 2014). In this context, model output supports and resonates with recent evidence of expansive marine-based

limits found on Porcupine Bank, west of Ireland (Peters et al., 2015), and at the Celtic Sea shelf break south of Ireland (Praeg et al., 2015). However, our model results presented here indicate that these far-field limits likely relate to short-lived surge-phases of ice stream activity, associated with enhanced orographic precipitation input to the Irish ice sheet, rather than long-term stable ice-sheet limits.

The limited duration of coalescence of the FIS and CIS in the North Sea is a significant conundrum for our optimal reconstruction. Although a variety of climate and oceanographic parameter modifications yield large-scale ice advance and extension along the entire North Sea shelf break (Fig. 6), including across Shetland and beyond (cf., Hall, 2013), the induced buttressing effects also force concomitant expansion of ice across Denmark and beyond. The inclusion of lateral shear stresses in the modelled stress balance may partially resolve these issues to the south for the Norwegian Channel ice stream, as may the inclusion of floating ice, in forcing different margin behaviour during coupling of the ice sheets. However, what the experiments reveal is that once the grounded margins merge, a principal east-west ice divide develops between Norway and Scotland, imposing significant diversions on pre-existing ice flow and stabilisation of the developed North Sea ice flow complex. While this development aligns with the most recent literature on North Sea ice coalescence (Sejrup et al., 2016), the subsequent deglaciation does not. Break-up of ice in this sector is thought to have initiated through unzipping of both ice sheets triggered by rapid drawdown of ice and grounding line retreat of

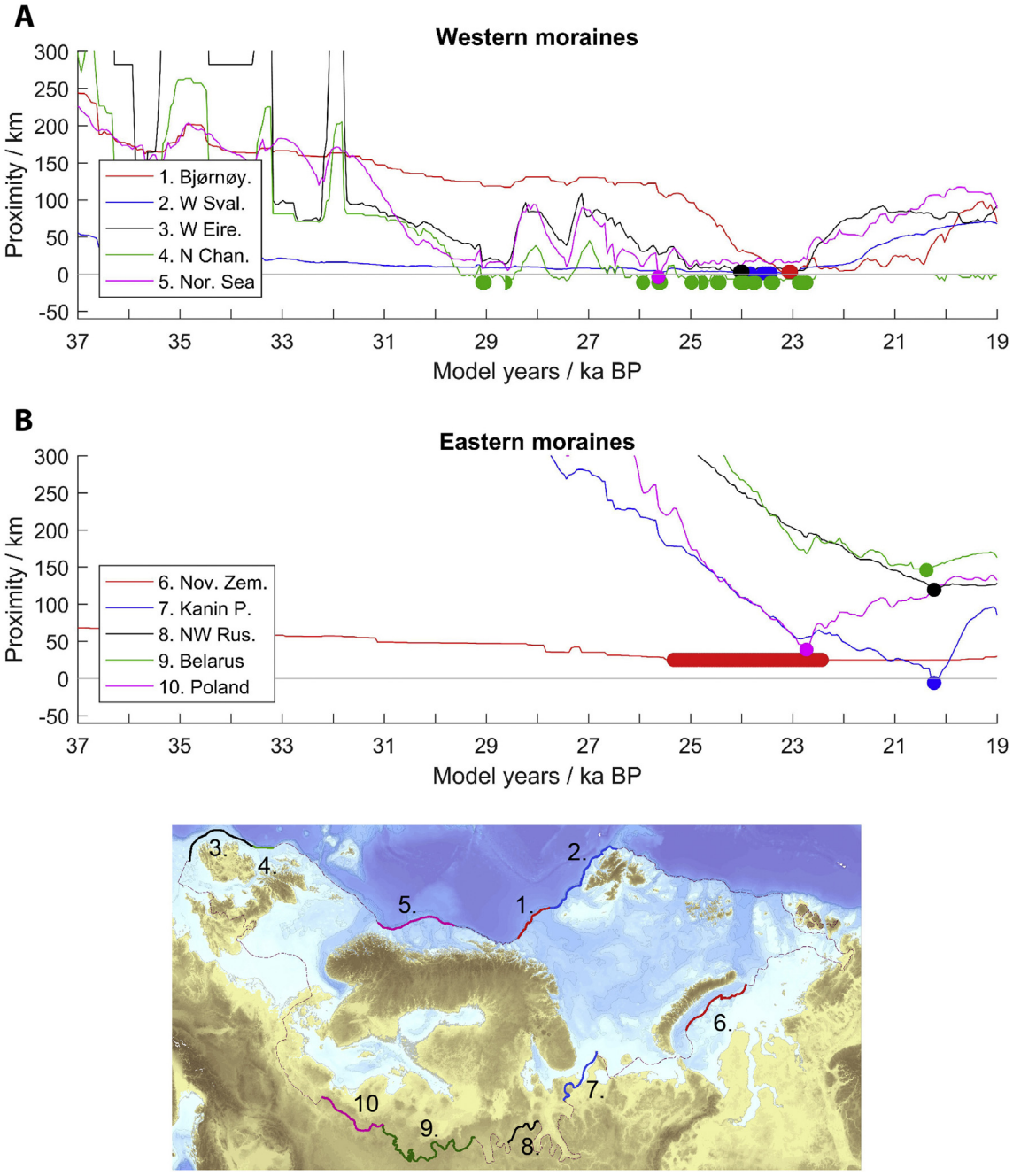

Fig. 8. (A, B) Proximity of modelled mean position (line), and point of maximum extension (circle), of western and eastern margins, respectively, to (C) regional limits of the EISC, following the "Automated Proximity and Conformity Analysis" (Napieralski et al., 2006). A full proximity and conformity analysis is included in Supplementary Figure S1.

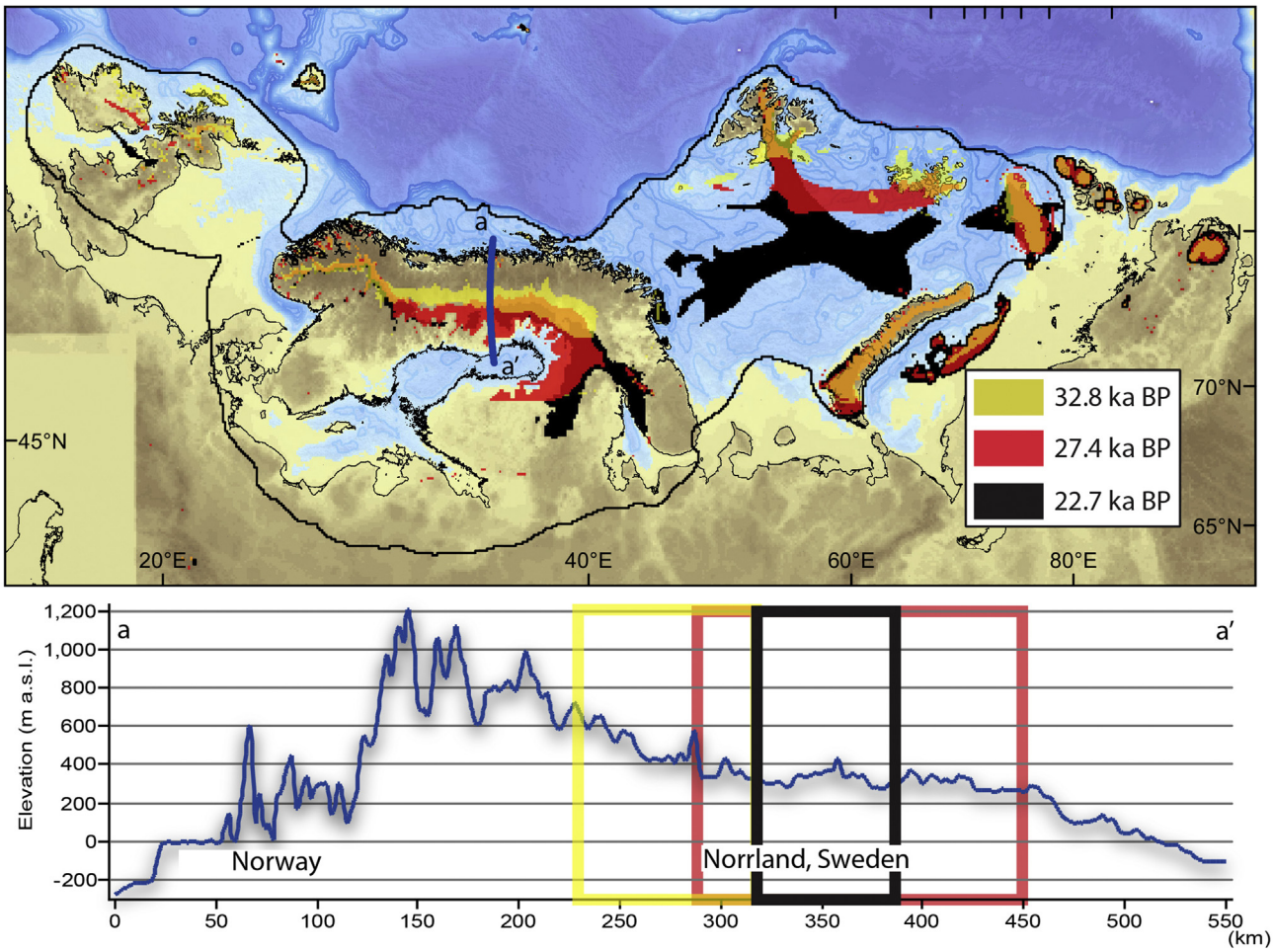

Fig. 9. Ice-divide regions (defined as areas of ice flow < 20 m a^{-1}) at 32.8, 27.4 and 22.7 ka BP, during the build-up of the ice-sheet complex. A successive eastward migration of the central ice divide is illustrated along cross profile a-a'. Its most eastward location, just inbound from the current Swedish coastline, matches closely that of the LGM ice divide location by Kleman et al. (2008).

the Norwegian Channel Ice Stream, amplified by catastrophic lake drainage c. 19 ka BP (Sejrup et al., 2016). Such a dynamic – marine based – instability is not reproduced in our optimal reconstruction, and with other diverging hypotheses on the breakup of this sector (e.g., Bradwell et al., 2008; Clark et al., 2012; Svendsen et al., 2015; Merritt et al., 2016), it is evident that how the FIS and CIS interacted and subsequently parted will be a glaciological problem for future modellers.

6.2. Asynchronous development

6.2.1. Maximum extension (west versus east)

Uncertainty over ice extents during the Ålesund/Tolsta interstadial (MIS 3/2 transition) has led to a variety of hypotheses being posited regarding initial growth and nucleation of the EISC, especially so for the marine-based BSIS where useful observations from this early stage are limited. Hypotheses range from the thickening of sea ice to depths required for grounding (Denton and Hughes, 1981; Hughes, 1987), the convergence of fringing ice shelves that eventually thickened in response to widespread buttressing against localised zones of grounding (Peyaud et al., 2007), and also the expansion and merging of terrestrial based ice caps concurrent with falling sea levels (Kvasov, 1978; Elverhøi et al., 1993). While floating ice shelves are not accounted for in the ice sheet model, the development of this ice sheet favours the latter premise, with growth of ice occurring rapidly across sub-aerial sectors of the Barents Sea, including the shallow bank areas that would have surfaced during the MIS 3 eustatic sea-level lowering (Fig. 4).

Peaks in total ice extent (5.48×10^6 km^2) and volume (7.18×10^6 km^3) in the optimum experiment occur c. 22.7 ka BP, approximately in the middle of the global LGM timeframe (26.5–19.0 ka BP) (Clark et al., 2009). However, the exact timing of maximum extension, both in the model and inferred from empirical data, varies significantly between different regions of the EISC (e.g., Larsen et al., 1999; Winsborrow et al., 2010; Clark et al., 2012; Hughes et al., 2016; Stroeven et al., 2016). Using the "Automated Proximity and Conformity Analysis" tools developed by Napieralski et al. (2006, 2007) and Li et al. (2008), the timing of ice incursion into individual sectors of the ice-sheet complex can be extracted from model output (Fig. 8).

The greatest differences occur between regions west and east in the domain, reflecting the close proximity of the shelf break to the major nucleation centres along the entire western margin. For example, the ice fronts west of Svalbard, Norway, and the United Kingdom (zones 2–5) are already within 20 km of the shelf break by c. 29 ka BP, and attain a maximum position between 23 and 25 ka BP following minor fluctuations (Fig. 8A). In contrast, to the east, ice-sheet incursion is more punctuated, reflecting the slow spread of the ice complex across much greater distances than possible along the western flanks. Peak glaciation in sectors such as NW

Russia and eastern Europe (zones 7–9) therefore occurs significantly later, between 20 and 21 ka BP (Fig. 8B). This asynchrony in maximum extension is commonly attributed to the migration of ice divides (Stroeven et al., 2016), reflecting changes in mass balance and flow regime across the ice sheet as well as the influence of the underlying topography (e.g., Larsen et al., 1999). By mapping the distribution of stable (<20 m a^{-1}) ice during the build-up of the ice complex it is possible to infer factors responsible for asymmetric development (Fig. 9).

The relatively small nucleation areas of the Celtic sectors leave little room for changes noticeable at the resolution of the modelled output – ice divides appear largely static up until the LGM, centred over the high ground of the Scottish Highlands and northern England and dictated by major flow through the North Channel and Irish Sea. More pronounced ice divide migrations are seen in Fennoscandia. Persistent ice drainage through the Norwegian Channel and fjords of southwest Norway keeps the ice divide centred over the high ground of the southern Scandes. However, further north, the dominating drawdown effect from the Baltic Sea ice stream forces the central ice divide to form east of these mountains across Norrland, Sweden (cf. Kleman et al., 2008). Furthermore, the late maximum extension into NW Russia (Fig. 8B) appears to result from the large hinging effect of the easternmost dogleg of the central ice divide northwards over Finland, concomitant with expansion of ice into the southeast Barents Sea (Fig. 9).

Nevertheless, it is the evolution of the drainage patterns in the Barents Sea that shows the greatest dynamics of all, reflecting the style of ice sheet growth and limited relief of this region. As the isolated ice caps expand and eventually merge, the principal junction migrates c. 600 km east towards Sentraldjupet by 20.3 ka BP (Fig. 9), dictated by significant ice drainage north and west via the Franz Victoria and Coast Parallel troughs and Bjørnøyrenna in particular (Fig. 2H).

6.2.2. LGM flowsets

A valuable data record for validating or constraining the evolution of numerical reconstructions is the palimpsest of ice-flow directions recorded by generations of glacial lineations and striations. The packaging of individual landforms into spatially delineated flowsets that mark patterns of ice flow during glaciation, has been applied rigorously to the EISC domain (e.g., Kleman et al., 1997; Winsborrow et al., 2010; Hughes et al., 2014). Here, we compare model output with flowsets reported from the Fennoscandian and southern Barents Sea domain that have been attributed with an LGM age based on location and relative positioning (Fig. 10).

Flowsets 1–5 located on the southern periphery of the FIS generally align well with the divergent flow of the Baltic Sea ice stream. Further north, flowsets 6–8 indicating flow westwards through the Scandes align closely and indicate flow perpendicular to the central ice divide, highlighting the topographic control on ice-drainage patterns in this sector. Flowset 9 at the head of the Baltic Sea ice stream, originally mapped as indicating northwards ice flow based on striae and till fabric (Kleman et al., 1997; Hättestrand, 1998), straddles the modelled ice divide throughout the LGM period. Landforms located here, therefore, may instead reflect an older or younger flow event that evacuated ice to the north (cf. Kleman et al., 1997), or that our optimum experiment falls short in describing the optimal ice divide location for this sector. An onset zone for ice streaming through the Gulf of Bothnia c. 350 km further south has been revealed from recent geomorphological mapping of multibeam bathymetry, though this is considered to relate to a late-stage (post Younger Dryas) flow event (Greenwood et al., 2015).

The increasing influence of eastwards migration of the ice sheet complex on concomitant ice-divide migration (Fig. 9) plays a crucial role on the timing of dominant flow through some major catchments towards the Barents Sea. Two notable examples include ice discharge circumnavigating the Varanger Peninsula (flowset 14), and to a lesser extent through the White Sea (flowset 15) (Fig. 10). The general pattern of ice flow around the Kola Peninsula resonates well with empirically based reconstructions, including a White Sea lobe that circumnavigates the peninsula through the White Sea Throat, and ice overrunning the peninsula in a north-easterly direction during the glacial maximum (Hättestrand et al., 2007). However, the growth of a cold-based and semi-independent ice cap on the Kola Peninsula during ice-sheet build-up is not reproduced, leading the model unable to reproduce the geomorphological footprint of the Keiva ice-marginal zone that follows the eastern coastline of the peninsula (Hättestrand and Clark, 2006; Hättestrand et al., 2007; Winsborrow et al., 2010). Ice discharging Bjørnøyrenna (flowset 12) is generally consistent from the north, though contributions from the central Barents Sea again are dependent on the position of the central ice divide here. Other flowsets, for example, through Håkjerringdjupet (flowset 13) and Ingøydjupet (flowset 11) are relatively consistent with both model timeslices, reflecting the topographic control on ice flow in proximity to the ice margin.

6.3. A thick or thin ice complex?

Constraints on the vertical extent of former ice sheets can be typically deduced from the distribution of isostatic rebound rates (e.g., Forman et al., 2004), as well as from the use of cosmogenic-nuclide exposure dating of erratic boulders or bedrock (e.g., Brook et al., 1996; Fabel et al., 2002; Stroeven et al., 2006; Goodfellow et al., 2014). With increasing sophistication of glacial-isostatic adjustment models (Auriac et al., 2016) and an ever-growing database of absolute dates (Hughes et al., 2011; Cuzzone et al., 2016; Hughes et al., 2016; Stroeven et al., 2016), estimations of minimum ice-thickness values across the EISC are in continual refinement. To examine the vertical accuracy of our modelled reconstruction, we compare the predicted LGM isostatic footprint and profile transects of the ice sheet with established empirical data.

6.3.1. Cosmogenic exposure age dating

As the optimum ice sheet experiment is driven by a relatively high “flow enhancement” factor of 50 (where ice is effectively “softer”), ice thickness values tend to be lower resulting in generally low-aspect ice-sheet profiles (Table 5). However, when compared to cosmogenic-exposure age sites at contrasting localities, the optimum model experiment remains within the realms of probability. The first transect (Fig. 11A, D), along the centreline of a major trough draining NW Svalbard, shows the LGM ice surface to be consistently above erratic boulders deposited on mountain flanks post-LGM. Further inland, old exposure dates indicate warm-based ice did not cover the highest peaks of NW Svalbard during the Late Weichselian (Gjermundsen et al., 2013), with the model suggesting at least Kongen was a potential nunatak for much, if not all, of the LGM.

The second transect over Sweden covers the central sector of the EISC, where the ice surface reached elevations close to its maximum altitude (Fig. 11B, E). The significant majority of cosmogenic exposure ages sampled from bedrock in this region exhibit various degrees of nuclide inheritance (Stroeven et al., 2006), indicating these mountain summits experienced negligible erosion during the last glaciation. Based on the abundance of these “old” cosmogenic exposure ages, in contrast with the younger deglaciation ages of erratic boulders, these bedrock surfaces have been speculated to have been permanently frozen, experiencing short

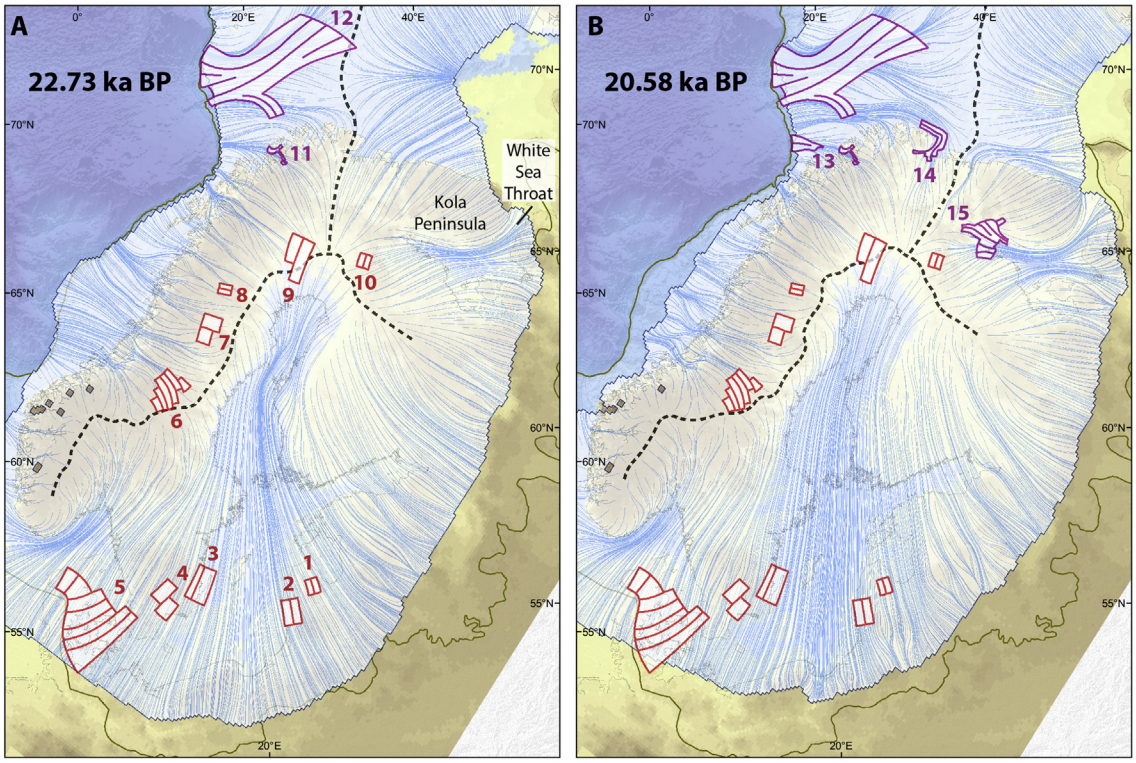

Fig. 10. Comparison of modelled surface flowlines at 22.73 ka BP (westerly dominated extension) and 20.58 ka BP (easterly dominated extension) with flowsets attributed to be of LGM age. Sources: red - Kleman et al. (1997); purple – Winsborrow et al. (2010). (For interpretation of the references to colour in this figure legend, the reader is referred to the web version of this article.)

periods of sliding only during deglaciation (Fabel et al., 2002; Harbor et al., 2006).

The final transect over southern Norway (Fig. 11C, F) extends from the present coastline to the central ice divide of the ice sheet. Again, the optimum model surface covers all erratic boulders of Late Weichselian age, but falls below the dated blockfield of Skåla, further supporting inferences that this summit and other coastal mountains were ice-free at the LGM (Brook et al., 1996; Goehring et al., 2008).

With respect to previously published ice reconstructions, all transects reveal the model by Siegert and Dowdeswell (2004) to have produced a minimum-style ice cover, generally reproducing the lowest-aspect ice sheet surface for all localities. Conversely, the glacial-isostatic adjustment modelling of Peltier (2004) and Peltier et al. (2015) (ICE-5G and ICE-6G_C, respectively) predicted significantly thicker ice, particularly at the ice margins, although these profiles are still generally consistent with all the dates collected so far. Based on these three transects of absolute dates, it thus appears that the optimum experiment presented here represents an intermediate-style LGM reconstruction, satisfying ice thickness predictions made through cosmogenic exposure dating.

6.3.2. Isostasy

Maximum glacial-isostatic adjustment beneath the LGM EISC is closely aligned with areas of ice-sheet nucleation, namely over the Scottish Highlands, northern Fennoscandia, and the north-west Barents Sea (Fig. 12). Although limited empirical data constrain crustal rebound across the Barents Sea, the modelled pattern of loading up to 290 m east of Svalbard at the LGM closely matches estimated patterns of uplift around Svalbard and Franz Josef Land (Forman et al., 2004) since 9000 ^{14}C ka BP (Fig. 12). Measurements of present-day glacial isostatic adjustment over Fennoscandia (1892–1991) reveal maximum rates of uplift occurring over the northern Baltic Sea (Mörner, 1990; Ekman, 1996; Milne et al., 2001). Although this is slightly south and east of the c. 290 m of depression predicted for 21 ka BP (Fig. 12), late deglaciation of ice from north-west Russia probably enhanced deformation of the Baltic Shield further east post-LGM.

Crustal deformation across Celtic sectors is relatively moderate, up to c. 125 m over the Scottish Highlands, reflecting the marginality of glaciation in this sector of the ice complex. Relative sea-level data from the British Isles and Ireland tend to support low-aspect ice streams draining a relatively thin ice centre over north-west Scotland (Lambeck, 1993; Kuchar et al., 2012). In contrast to previous ice-sheet modelling by Hubbard et al. (2009), predicted ice thickness values vary significantly across this sector, by up to 900 m compared to their maximal reconstruction. Furthermore, the location of greatest loading at the LGM lies much further west, above the west coast of Scotland. While these differences represent key improvements in matching relative sea-level data from eastern Scotland (Lambeck, 1993), interpreting the effects of non-local ice in Fennoscandia on the regional glacial rebound here is still highly unknown (Kuchar et al., 2012). Further model-comparison studies that take into account full glaciation of the Eurasian domain (e.g., Auriac et al., 2016), as well as a detailed chronology for the pace of ice retreat (e.g., Cuzzone et al., 2016), are thus needed to fully reconcile the spatially complex relative sea-level history of northern Eurasia.

6.4. Landscape impact of the LGM ice complex

Through mechanical interaction with the underlying topography, ice sheets play a powerful role in landscape evolution. Subglacial erosion processes are strongly associated with zones of

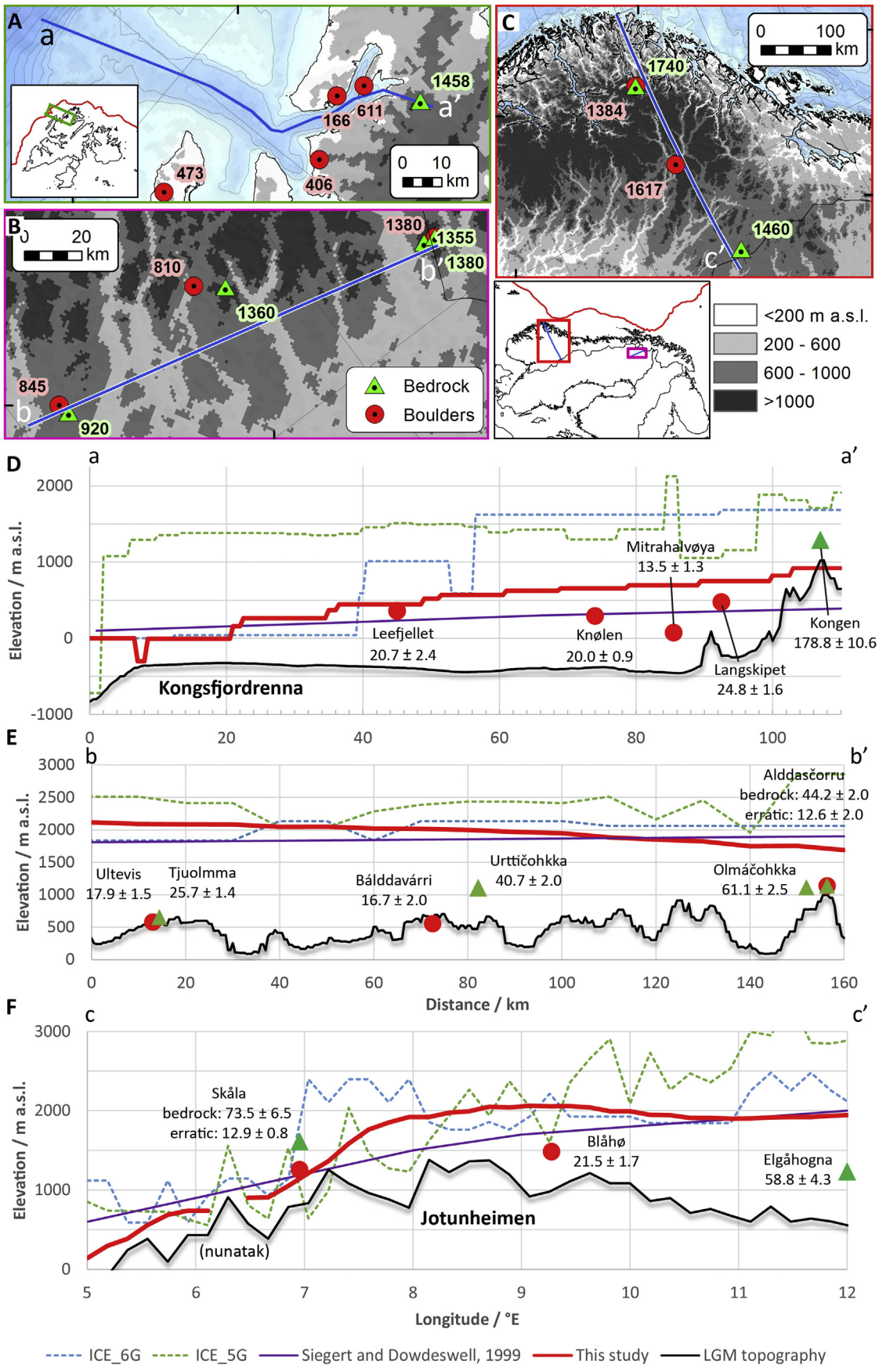

Fig. 11. Cosmogenic exposure-age transects over A) northwest Svalbard, B) northern Sweden, and C) southern Norway (Jotunheimen). Labels refer to the present-day elevation (m a.s.l.) of dated boulders and bedrock (Brook et al., 1996; Fabel et al., 2002; Harbor et al., 2006; Linge et al., 2006; Goehring et al., 2008; Gjermundsen et al., 2013; Landvik et al., 2013; Henriksen et al., 2014). D–F) Modelled surface profiles of the LGM ice sheet (ICE-5G v1.2 - Peltier, 2004; Siegert and Dowdeswell, 2004; ICE-6G_C - Peltier et al., 2015) and from this study (22.7 ka BP) in relation to dated sample positions. Cosmogenic exposure ages from Fennoscandia have been recalculated according to the Lal/Stone scaling scheme (Lal, 1991; Stone, 2000) by Stroeven et al. (2016), while those on Svalbard remain the same as originally reported in the literature. Bed topography and sample elevations in D-F have been isostatically adjusted according to model output from our optimum reconstruction.

fast-flowing, warm-based ice, amplified by the presence of subglacial meltwater. A common and simple method used in glacial erosion models therefore is to assume that the erosion rate is proportional to the ice-sliding velocity (e.g., Hallet, 1979; Oerlemans, 1984; Harbor et al., 1988; Amundson and Iverson, 2006; Herman et al., 2011). In our study, the erosion potential exerted by the ice, *EP*, at a fixed point on the glacier bed is given by:

$$EP = fV_b^2,$$

where the basal motion, V_b, is squared (e.g., Harbor et al., 1988) and f is an erosion constant that assumes the bedrock "erodibility" to be constant across the domain (Fig. 13). However, this adopted equation hugely simplifies the physical processes of basal erosion by excluding boundary conditions such as spatial variation in bedrock hardness, basal water pressure, particle–bed contact forces, and basal debris concentrations. These simplifications also fail to take into account some basic processes that can impact the effectiveness of glacial erosion, such as bedrock preconditioning, rock fracturing, joint exploitation, and debris entrainment.

While actual erosion rates are thus likely to have differed from the potential values predicted, the broad spatial pattern is of interest and reveals strong variations related to the timing and persistence of ice at the pressure melting point. For much of the Celtic and southern Fennoscandia sectors, subglacial erosion is widespread leading up to the LGM, particularly in the troughs which tend to focus fast-flowing ice. The relatively quick initiation of the Baltic, Norwegian Channel and west Norwegian ice streams after 30 ka BP make these areas particularly susceptible.

In the Barents Sea, only in the largest troughs such as Bjørnøyrenna and the Coast Parallel Trough do any instances of subglacial erosion appear probable during ice-sheet build-up. Importantly, these zones also coincide with areas of known gas hydrate destabilization (Chand et al., 2012; Winsborrow et al., 2016), making these critical sites for studying ice-hydrate interactions on glacial timescales (e.g., Kvenvolden, 1993; Rachold et al., 2007; Serov et al., 2015). Model scenarios and geophysical evidence point towards the existence of a 500 m-thick gas hydrate stability zone on the western Svalbard margin during the LGM, even under conservative estimates of ice thickness, with subsequent methane gas release occurring over many millennia associated with post-glacial climate warming and hydrate destabilization (Crémière et al., 2016; Portnov et al., 2016; Winsborrow et al., 2016). However, vast areas of the Barents and Kara seas are otherwise dominated by persistent cold-based conditions and creep-style deformation, enforced by perennial MAATs far below 0 °C. Permanently frozen conditions across much of the eastern Barents and Kara seas (Fig. 13) indicate that pre-Late Weichselian sediments and landforms in these areas may still be well-preserved.

Although to a lesser extent, frozen bed conditions are also widespread across the upland regions of Fennoscandia. The detailed mapping of glacial landforms and relict landscapes across this domain has revealed distinct patterns of Quaternary ice-sheet erosion, linked to the subglacial thermal organisation of successive ice sheets (Kleman, 1994; Kleman and Hättestrand, 1999; Kleman et al., 2008). Within central areas of the FIS there exists extension regions of pre-Late Weichselian glacial and non-glacial landforms, such as boulder fields, that have escaped destruction despite complete ice inundation over several tens of millennia (Fig. 13). Many of these areas align well with predicted zones of permanently cold-based ice or very low rates of potential erosion during the LGM. Based on the distribution of ribbed moraines, suggested to form via the brittle fracture of drift sheets and indicative of a transition from frozen- to thawed-bed conditions, a more widespread zone of cold-based conditions in Fennoscandia has been inferred during the LGM (Kleman and Hättestrand, 1999; Sarala, 2006; Stroeven et al., 2016) (Fig. 13). While the modelled basal temperatures across the Scandes aligns well with these empirical based predictions, strong discrepancies appear across the Baltic Sea and eastern Finland. This inconsistency is driven by the persistent penetration of the modelled Baltic Sea ice stream deep into the interior of the FIS, drawing down numerous fast-flowing tributaries and significantly raising the potential for erosion within neighbouring valleys. Further geomorphological mapping within the Baltic Sea is thus clearly needed to refine the subglacial thermal signature of the FIS and the onset zone of ice streaming in this region.

Studying and quantification of the basal processes operating beneath the EISC is critical for better understanding the role ice had on shaping the present-day landscape and sub-surface domain. Basal sliding within the model uses a Weertman (1964) sliding

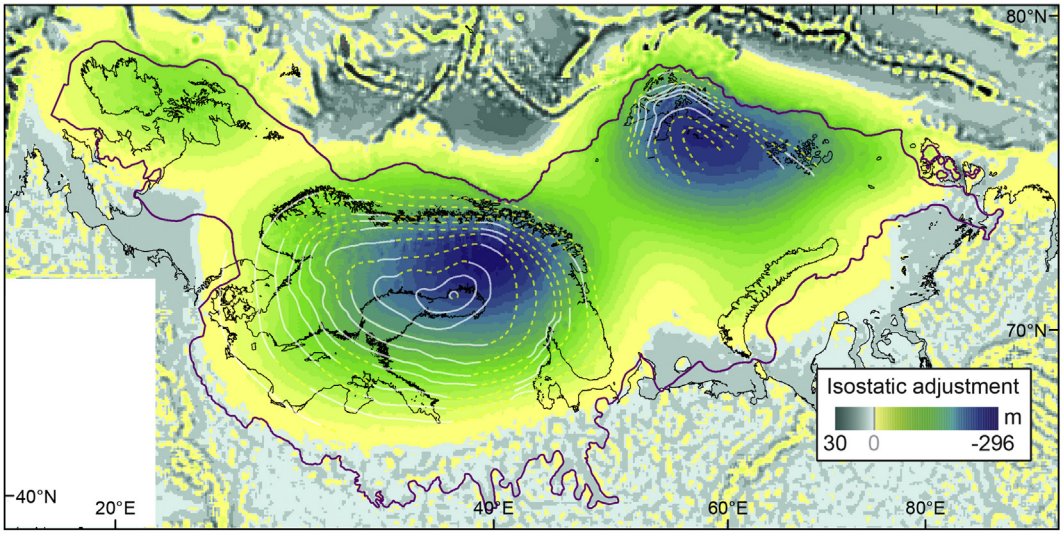

Fig. 12. Isostatic loading of the EISC at 21 ka BP, overlain by an estimated pattern of emergence isobases across the Barents Sea since 9000 ^{14}C yr (0–70 m; Forman et al., 2004)and since 1892 in Fennoscandia (1892–1991; −1 to 9 mm yr^{-1}; Ekman, 1996)(solid: measured; dashed: interpolated).

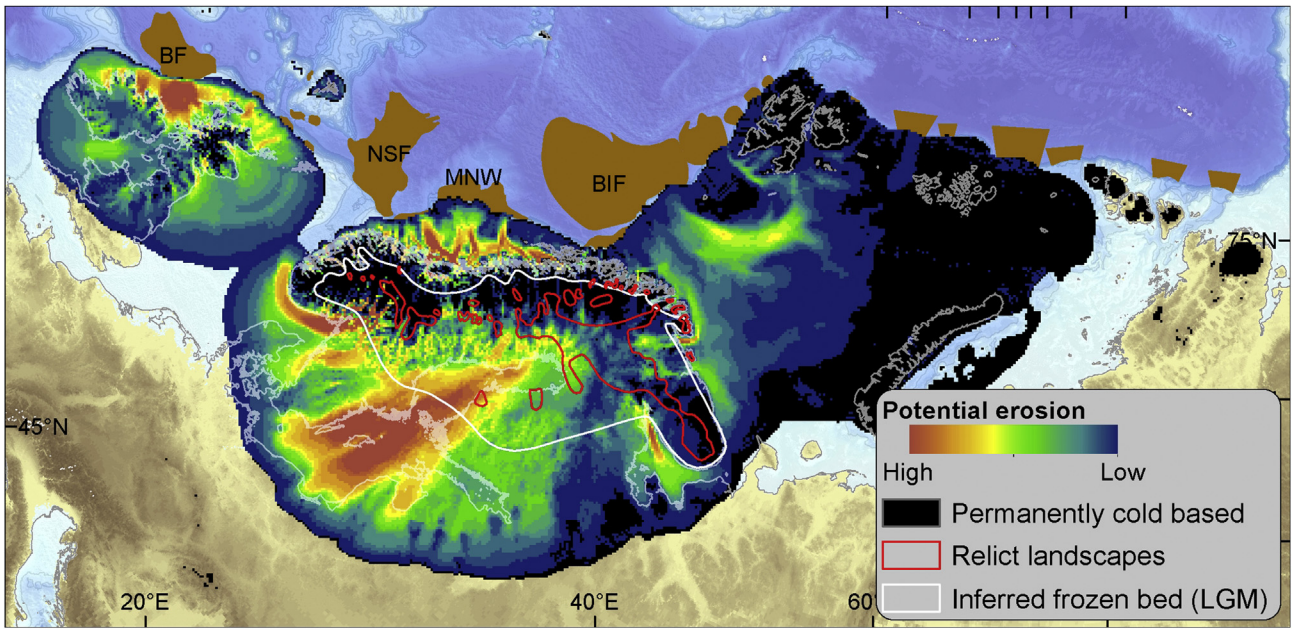

Fig. 13. Cumulative potential erosion between 37 and 19 ka BP. The outlines of relict landscapes across Fennoscandia (red) i.e. pre-Late Weichselian landforms and deposits such as boulder fields, are sourced from Kleman et al. (2008), and inferred frozen bed conditions (white) sourced from Stroeven et al. (2016). Locations of major glacial trough-mouth fans (brown) adapted from Dahlgren et al. (2005) and Batchelor and Dowdeswell (2014). BF: Barra and Donegal Fans; NSF: North Sea Fan; MNW: Mid Norway Wedge; BIF: Bear Island Fan. (For interpretation of the references to colour in this figure legend, the reader is referred to the web version of this article.)

relation that is triggered when the basal temperature approaches the pressure melting point (section 3.3). However, the distribution of subglacial meltwater is not modelled, and consequently the dependence of basal sliding on effective pressure is ignored. Herman et al. (2011) suggested that the inclusion of subglacial hydrology has the effect of reducing the effective pressure in the ablation area, which in turn leads to increased sliding and erosion below the equilibrium line altitude. Although this shortcoming would not significantly affect the broad pattern of potential erosion predicted (Fig. 13), it does indicate that the magnitude of difference in our predictions does not go far enough.

7. Conclusions

- In this study we use a higher-order, thermomechanical ice sheet model to reconstruct the build-up of the Last Glacial Maximum Eurasian ice-sheet complex (37–19 ka BP), as well as its sensitivity to a variety of key glaciological and climatological parameter configurations. Boundary condition data for each semi-independent ice centre are forced separately across three contrasting zones of the ice-sheet complex, reflecting the disparate oceanographic and climatological regimes of the northern Eurasian and High Arctic domains.
- The optimal experiment presented indicates rapid growth of the ice-sheet complex, with margins first present along much of the western Eurasian shelf break by 29 ka BP. The Celtic, Fennoscandian and Barents Sea ice sheets continue to expand south and east under further temperature cooling, reaching a peak extent and volume c. 22.7 ka BP (5.48×10^6 km^2 and 7.18×10^6 km^3 respectively).
- Required climate and oceanographic forcings differ significantly across the three ice sheet sub-domains, ranging from maritime conditions across Britain and Ireland to a polar desert regime in Siberia. Minimum temperature suppressions required to drive extensive glaciation decrease northwards, indicating an apparent insensitivity to climate cooling across Arctic regions. Considerable precipitation gradients that simulate rain-shadow effects are also required to keep ice within known empirical margins in eastern sectors. A heterogeneous sensitivity to calving losses is applied across the domain to simulate differences in sub-surface ocean temperature and the buttressing effects of perennial sea ice/ice shelves.
- Maximum LGM margins are not contemporaneous, with major ice-divide migrations forcing a relatively late incursion into eastern sectors c. 20–21 ka BP compared to c. 23–25 ka BP along western margins. Although rain-shadow effects amplify this asynchrony, the most compelling driver for this behaviour is a pronounced difference in topography either side of the major nucleation centres.
- Flowsets previously reported in the literature and attributed with an LGM age closely align with general predictions of ice flow direction across Fennoscandia and the southern Barents Sea. However, the relative chronologies of some flow packages appear to be closely associated with the timing of large magnitude ice-divide migrations as the ice complex migrated eastwards. Ice flow from central sectors of the BSIS and northern Fennoscandia therefore dominated only during the latter stages of the LGM.
- A relatively high enhancement factor of deformation ice flow is needed to force low-aspect growth of the ice complex, particularly for the Barents Sea ice sheet. Although the resulting ice cover is generally thinner than under conventional parameter values, comparison of ice profiles with cosmogenic-exposure age transects along the margins of Svalbard and Norway, as well as central Fennoscandia, reveal the optimum experiment to be a good fit, and an improvement on previous modelled reconstructions.
- Crustal deformation imposed by the EISC at 21 ka BP matches closely to the broad patterns of observed uplift across the northern Barents Sea and Fennoscandia. During the LGM, maximum depression by the ice sheet was c. 290 m east of Svalbard and in northern Sweden. More limited ice cover based

over the Scottish Highlands led to a maximum depression of c. 125 m.
- Subglacial properties of the model reconstructions reveal that basal erosion by the EISC was widespread at the LGM, particularly beneath the major ice streams that drained the Fennoscandian and Celtic ice sheets. Conversely, cold-based conditions dominated across the Barents Sea and upland regions of Fennoscandia. Such conditions across the hydrocarbon-rich continental shelf of the Eurasian Arctic would have created a stable environment conducive for the widespread growth of sub-marine gas hydrate as well as paraglacial permafrost.

Acknowledgements

The research is part of the Centre for Arctic Gas Hydrate, Environment and Climate, and was supported by the Research Council of Norway through its Centres of Excellence funding scheme (grant 223259), the PetroMaks project “Glaciations in the Barents Sea area (GlaciBar)” (grant 200672), and a Stockholm Uni SUCLIM consortium grant (to Stroeven) that supported Hubbard in the early development of the model code. We thank Adrian Hall for helpful comments on the manuscript. We also thank Caroline Clason and the editor Neil Glasser for their constructive feedback during the peer review process.

Appendix A. Supplementary data

Supplementary data related to this article can be found at http://dx.doi.org/10.1016/j.quascirev.2016.10.009.

References

Alexanderson, H., Adrielsson, L., Hjort, C., Möller, P., Antonov, O., Eriksson, S., Pavlov, M., 2002. Depositional history of the North Taymyr ice-marginal zone, Siberia-a landsystem approach. J. Quat. Sci. 17 (4), 361–382. http://dx.doi.org/10.1002/jqs.677.

Alexanderson, H., Johnsen, T., Murray, A.S., 2010. Re-dating the Pilgrimstad Interstadial with OSL: a warmer climate and a smaller ice sheet during the Swedish Middle Weichselian (MIS 3)? Boreas 39 (2), 367–376. http://dx.doi.org/10.1111/j.1502-3885.2009.00130.x.

Amundson, J.M., Iverson, N.R., 2006. Testing a glacial erosion rule using hang heights of hanging valleys, Jasper National Park, Alberta, Canada. J. Geophys. Res. Earth Surf. 111 (F1), F01020. http://dx.doi.org/10.1029/2005JF000359.

Amundson, J.M., Fahnestock, M., Truffer, M., Brown, J., Lüthi, M.P., Motyka, R.J., 2010. Ice mélange dynamics and implications for terminus stability, Jakobshavn Isbræ, Greenland. J. Geophys. Res. Earth Surf. 115 (F1), F01005. http://dx.doi.org/10.1029/2009JF001405.

Andersen, K.K., Azuma, N., Barnola, J.-M., Bigler, M., Biscaye, P., Caillon, N., Chappellaz, J., Clausen, H.B., Dahl-Jensen, D., Fischer, H., Flückiger, J., Fritzsche, D., Fujii, Y., Goto-Azuma, K., Grønvold, K., Gundestrup, N.S., Hansson, M., Huber, C., Hvidberg, C.S., Johnsen, S.J., Jonsell, U., Jouzel, J., Kipfstuhl, S., Landais, A., Leuenberger, M., Lorrain, R., Masson-Delmotte, V., Miller, H., Motoyama, H., Narita, H., Popp, T., Rasmussen, S.O., Raynaud, D., Rothlisberger, R., Ruth, U., Samyn, D., Schwander, J., Shoji, H., Siggard-Andersen, M.-L., Steffensen, J.P., Stocker, T., Sveinbjörnsdóttir, A.E., Svensson, A., Takata, M., Tison, J.-L., Thorsteinsson, T., Watanabe, O., Wilhelms, F., White, J.W.C., 2004. High-resolution record of Northern Hemisphere climate extending into the last interglacial period. Nature 431 (7005), 147–151. http://dx.doi.org/10.1038/nature02805.

Andreassen, K., Vorren, T.O., Johansen, K.B., 1985. Pre-late Weichselian glacimarine sediments at Arnøy, north Norway. Geol. Föreningen i Stockh. Förhandlingar 107 (1), 63–70. http://dx.doi.org/10.1080/11035898509452615.

Andreassen, K., Odegaard, C.M., Rafaelsen, B., 2007. Imprints of former ice streams, imaged and interpreted using industry three-dimensional seismic data from the south-western Barents Sea. Geol. Soc. Lond. Spec. Publ. 277 (1), 151–169. http://dx.doi.org/10.1144/GSL.SP.2007.277.01.09.

Arnold, N.S., van Andel, T.H., Valen, V., 2002. Extent and dynamics of the scandinavian ice sheet during oxygen isotope stage 3 (65,000–25,000 yr B.P.). Quat. Res. 57 (1), 38–48. http://dx.doi.org/10.1006/qres.2001.2298.

Auriac, A., Whitehouse, P.L., Bentley, M.J., Patton, H., Lloyd, J.M., Hubbard, A.L., 2016. Glacial isostatic adjustment associated with the Barents Sea ice sheet: a modelling inter-comparison. Quat. Sci. Rev. 147, 122–135. http://dx.doi.org/10.1016/j.quascirev.2016.02.011.

Barr, I.D., Clark, C.D., 2011. Glaciers and climate in Pacific Far NE Russia during the Last Glacial Maximum. J. Quat. Sci. 26 (2), 227–237. http://dx.doi.org/10.1002/jqs.1450.

Batchelor, C.L., Dowdeswell, J.A., 2014. The physiography of High Arctic cross-shelf troughs. Quat. Sci. Rev. 92, 68–96. http://dx.doi.org/10.1016/j.quascirev.2013.05.025.

Bauch, H.A., Erlenkeuser, H., Spielhagen, R.F., Struck, U., Matthiessen, J., Thiede, J., Heinemeier, J., 2001. A multiproxy reconstruction of the evolution of deep and surface waters in the subarctic Nordic seas over the last 30,000 yr. Quat. Sci. Rev. 20 (4), 659–678. http://dx.doi.org/10.1016/S0277-3791(00)00098-6.

Bjarnadóttir, L.R., Winsborrow, M.C.M., Andreassen, K., 2014. Deglaciation of the central Barents Sea. Quat. Sci. Rev. 92, 208–226. http://dx.doi.org/10.1016/j.quascirev.2013.09.012.

Blatter, H., 1995. Velocity and stress-fields in grounded glaciers - a simple algorithm for including deviatoric stress gradients. J. Glaciol. 41 (138), 333–344. http://dx.doi.org/10.3198/1995JoG41-138-333-344.

Bos, J.A.A., Dickson, J.H., Coope, G.R., Jardine, W.G., 2004. Flora, fauna and climate of Scotland during the Weichselian Middle Pleniglacial - palynological, macrofossil and coleopteran investigations. Palaeogeogr. Palaeoclimatol. Palaeoecol. 204 (1–2), 65–100. http://dx.doi.org/10.1016/S0031-0182(03)00724-7.

Boulton, G.S., Dongelmans, P.W., Punkari, M., Broadgate, M., 2001. Palaeoglaciology of an ice sheet through a glacial cycle: the European ice sheet through the Weichselian. Quat. Sci. Rev. 20 (4), 591–625. http://dx.doi.org/10.1016/S0277-3791(00)00160-8.

Bowen, D., Phillips, F., McCabe, A., Knutz, P., Sykes, G., 2002. New data for the Last Glacial Maximum in Great Britain and Ireland. Quat. Sci. Rev. 21 (1–3), 89–101. http://dx.doi.org/10.1016/S0277-3791(01)00102-0.

Box, J.E., Steffen, K., 2001. Sublimation on the Greenland Ice Sheet from automated weather station observations. J. Geophys. Res. Atmos. 106 (D24), 33965–33981. http://dx.doi.org/10.1029/2001JD900219.

Box, J.E., Bromwich, D.H., Bai, L., 2004. Greenland ice sheet surface mass balance 1991–2000: application of Polar MM5 mesoscale model and in situ data. J. Geophys. Res. Atmos. 109 (D16), D16105. http://dx.doi.org/10.1029/2003JD004451.

Bradwell, T., Stoker, M.S., Golledge, N.R., Wilson, C.K., Merritt, J.W., Long, D., Everest, J.D., Hestvik, O.B., Stevenson, A.G., Hubbard, A.L., Finlayson, A.G., Mathers, H.E., 2008. The northern sector of the last British Ice Sheet: maximum extent and demise. Earth-Science Rev. 88 (3–4), 207–226. http://dx.doi.org/10.1016/j.earscirev.2008.01.008.

Braithwaite, R.J., 1995. Positive degree-day factors for ablation on the Greenland ice sheet studied by energy-balance modelling. J. Glaciol. 41 (137), 153–160. http://dx.doi.org/10.3198/1995JoG41-137-153-160.

Briner, J.P., Goehring, B.M., Mangerud, J., Svendsen, J.I., 2016. The deep accumulation of ^{10}Be at Utsira, southwestern Norway: implications for cosmogenic nuclide exposure dating in peripheral ice sheet landscapes. Geophys. Res. Lett. 43 (17), 9121–9129. http://dx.doi.org/10.1002/2016GL070100.

Brook, E.J., Nesje, A., Lehman, S.J., Raisbeck, G.M., Yiou, F., 1996. Cosmogenic nuclide exposure ages along a vertical transect in western Norway: implications for the height of the Fennoscandian ice sheet. Geology 24 (3), 207–210. http://dx.doi.org/10.1130/0091-7613(1996)024<0207:CNEAAA>2.3.CO;2.

Brown, C.S., Meier, M.F., Post, A., 1982. Calving Speed of Alaskan Tidewater Glaciers, with Application to Columbia Glacier. US Geological Survey Professional Paper 1258-C.

Brown, E.J., Rose, J., Coope, R.G., Lowe, J.J., 2007. An MIS 3 age organic deposit from Balglass Burn, central Scotland: palaeoenvironmental significance and implications for the timing of the onset of the LGM ice sheet in the vicinity of the British Isles. J. Quat. Sci. 22 (3), 295–308. http://dx.doi.org/10.1002/jqs.1028.

Chand, S., Thorsnes, T., Rise, L., Brunstad, H., Stoddart, D., Bøe, R., Lågstad, P., Svolsbru, T., 2012. Multiple episodes of fluid flow in the SW Barents Sea (Loppa High) evidenced by gas flares, pockmarks and gas hydrate accumulation. Earth Planet. Sci. Lett. http://dx.doi.org/10.1016/j.epsl.2012.03.021.

Chandler, D.M., Hubbard, A.L., Hubbard, B.P., Nienow, P.W., 2006. A Monte Carlo error analysis for basal sliding velocity calculations. J. Geophys. Res. Earth Surf. 111 (F4), F04005. http://dx.doi.org/10.1029/2006JF000476.

Clark, P.U., Dyke, A.S., Shakun, J.D., Carlson, A.E., Clark, J., Wohlfarth, B., Mitrovica, J.X., Hostetler, S.W., McCabe, A.M., 2009. The Last Glacial Maximum. Science 325 (5941), 710–714. http://dx.doi.org/10.1126/science.1172873.

Clark, C.D., Hughes, A.L.C., Greenwood, S.L., Jordan, C., Sejrup, H.P., 2012. Pattern and timing of retreat of the last British-irish ice sheet. Quat. Sci. Rev. 44, 112–146. http://dx.doi.org/10.1016/j.quascirev.2010.07.019.

Clason, C.C., Applegate, P.J., Holmlund, P., 2014. Modelling Late Weichselian evolution of the Eurasian ice sheets forced by surface meltwater-enhanced basal sliding. J. Glaciol. 29–40. http://dx.doi.org/10.3189/2014JoG13J037.

Crémière, A., Lepland, A., Chand, S., Sahy, D., Condon, D.J., Noble, S.R., Martma, T., Thorsnes, T., Sauer, S., Brunstad, H., 2016. Timescales of methane seepage on the Norwegian margin following collapse of the Scandinavian Ice Sheet. Nat. Commun. 7, 11509. http://dx.doi.org/10.1038/ncomms11509.

Cuffey, K.M., Paterson, W.S.B., 2010. The Physics of Glaciers, fourth ed. Butterworth-Heinemann, Oxford.

Cuzzone, J.K., Clark, P.U., Carlson, A.E., Ullman, D.J., Rinterknecht, V.R., Milne, G.A., Lunkka, J.-P., Wohlfarth, B., Marcott, S.A., Caffee, M., 2016. Final deglaciation of the Scandinavian Ice Sheet and implications for the Holocene global sea-level budget. Earth Planet. Sci. Lett. http://dx.doi.org/10.1016/j.epsl.2016.05.019.

Dahlgren, K.I.T., Vorren, T.O., Stoker, M.S., Nielsen, T., Nygård, A., Sejrup, H.P., 2005. Late Cenozoic prograding wedges on the NW European continental margin: their formation and relationship to tectonics and climate. Mar. Petroleum Geol. 22 (9–10), 1089–1110. http://dx.doi.org/10.1016/j.marpetgeo.2004.12.008.

De Woul, M., Hock, R., 2005. Static mass-balance sensitivity of Arctic glaciers and ice caps using a degree-day approach. Ann. Glaciol. 42 (1), 217–224. http://

dx.doi.org/10.3189/172756405781813096.
Denton, G.H., Hughes, T.J., 1981. The Last Great Ice Sheets, the Last Great Ice Sheet. John Wiley, New York.
Déry, S.J., Yau, M.K., 2002. Large-scale mass balance effects of blowing snow and surface sublimation. J. Geophys. Res. Atmos. 107 (D23) http://dx.doi.org/10.1029/2001JD001251.
Dunlop, P., Shannon, R., McCabe, M., Quinn, R., Doyle, E., 2010. Marine geophysical evidence for ice sheet extension and recession on the Malin Shelf: new evidence for the western limits of the British Irish Ice Sheet. Mar. Geol. 276 (1–4), 86–99. http://dx.doi.org/10.1016/j.margeo.2010.07.010.
Ehlers, J., Gibbard, P.L., 2007. The extent and chronology of Cenozoic Global Glaciation. Quat. Int. 164–165, 6–20. http://dx.doi.org/10.1016/j.quaint.2006.10.008.
Ekman, M., 1996. A consistent map of the postglacial uplift of Fennoscandia. Terra Nova. 8 (2), 158–165. http://dx.doi.org/10.1111/j.1365-3121.1996.tb00739.x.
Elverhøi, A., Fjeldskaar, W., Solheim, A., Nyland-Berg, M., Russwurm, L., 1993. The Barents Sea Ice Sheet — A model of its growth and decay during the last ice maximum. Quat. Sci. Rev. 12 (10), 863–873. http://dx.doi.org/10.1016/0277-3791(93)90025-H.
Fabel, D., Stroeven, A.P., Harbor, J., Kleman, J., Elmore, D., Fink, D., 2002. Landscape preservation under Fennoscandian ice sheets determined from in situ produced ^{10}Be and ^{26}Al. Earth Planet. Sci. Lett. 201 (2), 397–406. http://dx.doi.org/10.1016/S0012-821X(02)00714-8.
Forman, S.L., Lubinski, D.J., Ingólfsson, Ó., Zeeberg, J.J., Snyder, J.A., Siegert, M.J., Matishov, G.G., 2004. A review of postglacial emergence on Svalbard, Franz Josef Land and Novaya Zemlya, northern Eurasia. Quat. Sci. Rev. 23 (11–13), 1391–1434. http://dx.doi.org/10.1016/j.quascirev.2003.12.007.
Forsström, P.-L., Greve, R., 2004. Simulation of the Eurasian ice sheet dynamics during the last glaciation. Glob. Planet. Change 42 (1–4), 59–81. http://dx.doi.org/10.1016/j.gloplacha.2003.11.003.
Fowler, A.C., 1986. Sub-temperate basal sliding. J. Glaciol. 32 (110), 3–5. http://dx.doi.org/10.3198/1986JoG32-110-3-5.
Fredin, O., Rubensdotter, L., van Welden, A., Larsen, E., Lysså, A., 2012. Distribution of ice marginal moraines in NW Russia. J. Maps 8 (3), 236–241. http://dx.doi.org/10.1080/17445647.2012.708536.
Fujii, Y., Kusunoki, K., 1982. The role of sublimation and condensation in the formation of ice sheet surface at Mizuho Station, Antarctica. J. Geophys. Res. Oceans 87 (C6), 4293–4300. http://dx.doi.org/10.1029/JC087iC06p04293.
Gjermundsen, E.F., Briner, J.P., Akçar, N., Salvigsen, O., Kubik, P., Gantert, N., Hormes, A., 2013. Late Weichselian local ice dome configuration and chronology in Northwestern Svalbard: early thinning, late retreat. Quat. Sci. Rev. 72, 112–127. http://dx.doi.org/10.1016/j.quascirev.2013.04.006.
Goehring, B.M., Brook, E.J., Linge, H., Raisbeck, G.M., Yiou, F., 2008. Beryllium-10 exposure ages of erratic boulders in southern Norway and implications for the history of the Fennoscandian Ice Sheet. Quat. Sci. Rev. 27 (3–4), 320–336. http://dx.doi.org/10.1016/j.quascirev.2007.11.004.
Golledge, N.R., Hubbard, A.L., Sugden, D.E., 2009. Mass balance, flow and subglacial processes of a modelled Younger Dryas ice cap in Scotland. J. Glaciol. 55 (189), 32–42. http://dx.doi.org/10.3189/002214309788608967.
Golledge, N., Hubbard, A., Bradwell, T., 2010. Influence of seasonality on glacier mass balance, and implications for palaeoclimate reconstructions. Clim. Dyn. 35 (5), 757–770. http://dx.doi.org/10.1007/s00382-009-0616-6.
Golledge, N.R., Mackintosh, A.N., Anderson, B.M., Buckley, K.M., Doughty, A.M., Barrell, D.J.A., Denton, G.H., Vandergoes, M.J., Andersen, B.G., Schaefer, J.M., 2012. Last Glacial Maximum climate in New Zealand inferred from a modelled southern Alps icefield. Quat. Sci. Rev. 46, 30–45. http://dx.doi.org/10.1016/j.quascirev.2012.05.004.
Goodfellow, B.W., Stroeven, A.P., Fabel, D., Fredin, O., Derron, M.-H., Bintanja, R., Caffee, M.W., 2014. Arctic–alpine blockfields in the northern Swedish Scandes: late Quaternary - not Neogene. Earth Surf. Dyn. 2 (2), 383–401. http://dx.doi.org/10.5194/esurf-2-383-2014.
Greenwood, S.L., Clark, C.D., 2009. Reconstructing the last Irish Ice Sheet 2: a geomorphologically-driven model of ice sheet growth, retreat and dynamics. Quat. Sci. Rev. 28 (27–28), 3101–3123. http://dx.doi.org/10.1016/j.quascirev.2009.09.014.
Greenwood, S.L., Clason, C.C., Mikko, H., Nyberg, J., Peterson, G., Smith, C.A., 2015. Integrated use of LiDAR and multibeam bathymetry reveals onset of ice streaming in the northern Bothnian Sea. J. Geol. Soc. Swed. 137 (4), 284–292. http://dx.doi.org/10.1080/11035897.2015.1055513.
Hald, M., Sættem, J., Nesse, E., 1990. Middle and Late Weichselian stratigraphy in shallow drillings from the southwestern Barents Sea: foraminiferal, amino acid and radiocarbon evidence. Nor. J. Geol. 70 (4), 241–257.
Hall, A.M., 2013. The last glaciation of Shetland: local ice cap or invasive ice sheet? Nor. J. Geol. 93 (3–4), 229–242.
Hallet, B., 1979. A theoretical model of glacial abrasion. J. Glaciol. 23, 39–50. http://dx.doi.org/10.3198/1979JoG23-89-39-50.
Harbor, J.M., Hallet, B., Raymond, C.F., 1988. A numerical model of landform development by glacial erosion. Nature 333, 347–349. http://dx.doi.org/10.1038/333347a0.
Harbor, J., Stroeven, A.P., Fabel, D., Clarhäll, A., Kleman, J., Li, Y., Elmore, D., Fink, D., 2006. Cosmogenic nuclide evidence for minimal erosion across two subglacial sliding boundaries of the late glacial Fennoscandian ice sheet. Geomorphology 75 (1), 90–99. http://dx.doi.org/10.1016/j.geomorph.2004.09.036.
Hättestrand, C., 1998. The glacial geomorphology of central and northern Sweden. Sveriges Geol. Undersökning, Ca. 85, 1–47.
Hättestrand, C., Clark, C.D., 2006. The glacial geomorphology of Kola Peninsula and adjacent areas in the Murmansk Region, Russia. J. Maps 2 (1), 30–42. http://dx.doi.org/10.4113/jom.2006.41.
Hättestrand, C., Kolka, V., Stroeven, A., 2007. The Keiva ice marginal zone on the Kola Peninsula, northwest Russia: a key component for reconstructing the palaeoglaciology of the northeastern Fennoscandian Ice Sheet. Boreas 36 (4), 352–370. http://dx.doi.org/10.1080/03009480701317488.
Hebbeln, D., Dokken, T., Andersen, E.S., Hald, M., Elverhøi, A., 1994. Moisture supply for northern ice-sheet growth during the Last Glacial Maximum. Nature 370, 357–360. http://dx.doi.org/10.1038/370357a0.
Helmens, K.F., 2014. The Last Interglacial–Glacial cycle (MIS 5–2) re-examined based on long proxy records from central and northern Europe. Quat. Sci. Rev. 86, 115–143. http://dx.doi.org/10.1016/j.quascirev.2013.12.012.
Helmens, K.F., Engels, S., 2010. Ice-free conditions in eastern Fennoscandia during early Marine Isotope Stage 3: lacustrine records. Boreas 39 (2), 399–409. http://dx.doi.org/10.1111/j.1502-3885.2010.00142.x.
Henriksen, M., Alexanderson, H., Landvik, J.Y., Linge, H., Peterson, G., 2014. Dynamics and retreat of the Late Weichselian Kongsfjorden ice stream, NW Svalbard. Quat. Sci. Rev. 92, 235–245. http://dx.doi.org/10.1016/j.quascirev.2013.10.035.
Herman, F., Beaud, F., Champagnac, J.D., Lemieux, J.M., Sternai, P., 2011. Glacial hydrology and erosion patterns: a mechanism for carving glacial valleys. Earth Planet. Sci. Lett. 310 (3–4), 498–508. http://dx.doi.org/10.1016/j.epsl.2011.08.022.
Heyman, J., Stroeven, A.P., Harbor, J.M., Caffee, M.W., 2011. Too young or too old: evaluating cosmogenic exposure dating based on an analysis of compiled boulder exposure ages. Earth Planet. Sci. Lett. http://dx.doi.org/10.1016/j.epsl.2010.11.040.
Hibbert, F.D., Austin, W.E.N., Leng, M.J., Gatliff, R.W., 2010. British Ice Sheet dynamics inferred from North Atlantic ice-rafted debris records spanning the last 175 000 years. J. Quat. Sci. 25 (4), 461–482. http://dx.doi.org/10.1002/jqs.1331.
Hijmans, R.J., Cameron, S.E., Parra, J.L., Jones, P.G., Jarvis, A., 2005. Very high resolution interpolated climate surfaces for global land areas. Int. J. Climatol. 25 (15), 1965–1978. http://dx.doi.org/10.1002/joc.1276.
Hindmarsh, R.C.A., 2004. A numerical comparison of approximations to the Stokes equations used in ice sheet and glacier modeling. J. Geophys. Res. Earth Surf. 109 (F1), F01012. http://dx.doi.org/10.1029/2003JF000065.
Hindmarsh, R., Le Meur, E., 2001. Dynamical processes involved in the retreat of marine ice sheets. J. Glaciol. 47 (157), 271–282. http://dx.doi.org/10.3189/172756501781832269.
Hubbard, A., 1999. High-resolution modeling of the advance of the Younger Dryas ice sheet and its climate in Scotland. Quat. Res. 52 (1), 27–43. http://dx.doi.org/10.1006/qres.1999.2055.
Hubbard, A., 2000. The verification and significance of three approaches to longitudinal stresses in high-resolution models of glacier flow. Geogr. Ann. Ser. A, Phys. Geogr. 82 (4), 471–487. http://dx.doi.org/10.1111/j.0435-3676.2000.00135.x.
Hubbard, A., 2006. The validation and sensitivity of a model of the Icelandic ice sheet. Quat. Sci. Rev. 25 (17–18), 2297–2313. http://dx.doi.org/10.1016/j.quascirev.2006.04.005.
Hubbard, A., Blatter, H., Nienow, P., Mair, D., Hubbard, B., 1998. Comparison of a three-dimensional model for glacier flow with field data from Haut Glacier d'Arolla, Switzerland. J. Glaciol. 44 (147), 368–378. http://dx.doi.org/10.3198/1998JoG44-147-368-378.
Hubbard, B.P., Hubbard, A., Mader, H.M., Tison, J.-L., Grust, K., Nienow, P.W., 2003. Spatial variability in the water content and rheology of temperate glaciers: glacier de Tsanfleuron, Switzerland. Ann. Glaciol. 37 (1), 1–6. http://dx.doi.org/10.3189/172756403781815474.
Hubbard, A., Hein, A.S., Kaplan Michael, R., Hulton, N.R.J., Glasser, N.F., 2005. A modelling reconstruction of the Last Glacial Maximum ice sheet and its deglaciation in the vicinity of the Northern Patagonian Icefield, South America. Geogr. Ann. Ser. A, Phys. Geogr. 87 (2), 375–391. http://dx.doi.org/10.1111/j.0435-3676.2005.00264.x.
Hubbard, A., Bradwell, T., Golledge, N., Hall, A., Patton, H., Sugden, D., Cooper, R., Stoker, M., 2009. Dynamic cycles, ice streams and their impact on the extent, chronology and deglaciation of the British–Irish ice sheet. Quat. Sci. Rev. 28 (7–8), 758–776. http://dx.doi.org/10.1016/j.quascirev.2008.12.026.
Hubberten, H.W., Andreev, A., Astakhov, V.I., Demidov, I., Dowdeswell, J.A., Henriksen, M., Hjort, C., Houmark-Nielsen, M., Jakobsson, M., Kuzmina, S., Larsen, E., Lunkka, J.P., Lysså, A., Mangerud, J., Möller, P., Saarnisto, M., Schirrmeister, L., Sher, A.V., Siegert, C., Siegert, M.J., Svendsen, J.I., 2004. The periglacial climate and environment in northern Eurasia during the Last Glaciation. Quat. Sci. Rev. 23 (11–13), 1333–1357. http://dx.doi.org/10.1016/j.quascirev.2003.12.012.
Hughes, T., 1987. The marine ice transgression hypothesis. Geogr. Ann. Ser. A, Phys. Geogr. 69 (2), 237–250. http://dx.doi.org/10.2307/521185.
Hughes, A.L.C., Greenwood, S.L., Clark, C.D., 2011. Dating constraints on the last British-Irish Ice Sheet: a map and database. J. Maps 7 (1), 156–184. http://dx.doi.org/10.4113/jom.2011.1145.
Hughes, A.L.C., Clark, C.D., Jordan, C.J., 2014. Flow-pattern evolution of the last British Ice Sheet. Quat. Sci. Rev. 89, 148–168. http://dx.doi.org/10.1016/j.quascirev.2014.02.002.
Hughes, A.L.C., Gyllencreutz, R., Lohne, Ø.S., Mangerud, J., Svendsen, J.I., 2016. The last Eurasian ice sheets – a chronological database and time-slice reconstruction, DATED-1. Boreas 45 (1), 1–45. http://dx.doi.org/10.1111/bor.12142.
Huybrechts, P., Oerlemans, J., 1990. Response of the Antarctic ice sheet to future

greenhouse warming. Clim. Dyn. 5 (2), 93–102. http://dx.doi.org/10.1007/BF00207424.
Jacobi, R.M., Rose, J., MacLeod, A., Higham, T.F.G., 2009. Revised radiocarbon ages on woolly rhinoceros (*Coelodonta antiquitatis*) from western central Scotland: significance for timing the extinction of woolly rhinoceros in Britain and the onset of the LGM in central Scotland. Quat. Sci. Rev. 28 (25), 2551–2556. http://dx.doi.org/10.1016/j.quascirev.2009.08.010.
Jakobsson, M., Mayer, L., Coakley, B., Dowdeswell, J.A., Forbes, S., Fridman, B., Hodnesdal, H., Noormets, R., Pedersen, R., Rebesco, M., Schenke, H.W., Zarayskaya, Y., Accettella, D., Armstrong, A., Anderson, R.M., Bienhoff, P., Camerlenghi, A., Church, I., Edwards, M., Gardner, J.V., Hall, J.K., Hell, B., Hestvik, O., Kristoffersen, Y., Marcussen, C., Mohammad, R., Mosher, D., Nghiem, S.V., Pedrosa, M.T., Travaglini, P.G., Weatherall, P., 2012. The International Bathymetric Chart of the Arctic Ocean (IBCAO) version 3.0. Geophys. Res. Lett. 39 (12), L12609. http://dx.doi.org/10.1029/2012GL052219.
Jessen, S.P., Rasmussen, T.L., Nielsen, T., Solheim, A., 2010. A new Late Weichselian and Holocene marine chronology for the western Svalbard slope 30,000–0 cal years BP. Quat. Sci. Rev. 29 (9–10), 1301–1312. http://dx.doi.org/10.1016/j.quascirev.2010.02.020.
Jóhannesson, T., Sigurdsson, O., Laumann, T., Kennett, M., 1995. Degree-day glacier mass-balance modelling with applications to glaciers in Iceland, Norway and Greenland. J. Glaciol. 41 (138), 345–358. http://dx.doi.org/10.3198/1995JoG41-138-345-358.
Joughin, I., Howat, I.M., Fahnestock, M., Smith, B., Krabill, W., Alley, R.B., Stern, H., Truffer, M., 2008. Continued evolution of Jakobshavn Isbrae following its rapid speedup. J. Geophys. Res. Earth Surf. 113 (F4), F04006. http://dx.doi.org/10.1029/2008JF001023.
Kameda, T., Azuma, N., Furukawa, T., Ageta, Y., Takahashi, S., 1997. Surface mass balance, sublimation and snow temperatures at Dome Fuji Station, Antarctica, in 1995. Proc. NIPR Symposium Polar Meteorology Glaciol. 11, 24–34.
Kjær, K., Larsen, E., Funder, S., Demidov, I., Jensen, M., Håkansson, L., Murray, A., 2006. Eurasian ice-sheet interaction in northwestern Russia throughout the late Quaternary. Boreas 35 (3), 444–475. http://dx.doi.org/10.1080/03009480600781891.
Kleman, J., 1994. Preservation of landforms under ice sheets and ice caps. Geomorphology 9 (1), 19–32. http://dx.doi.org/10.1016/0169-555X(94)90028-0.
Kleman, J., Hättestrand, C., 1999. Frozen-bed Fennoscandian and Laurentide ice sheets during the Last Glacial Maximum. Nature 402 (6757), 63–66. http://dx.doi.org/10.1038/47005.
Kleman, J., Stroeven, A.P., 1997. Preglacial surface remnants and Quaternary glacial regimes in northwestern Sweden. Geomorphology 19 (1–2), 35–54. http://dx.doi.org/10.1016/S0169-555X(96)00046-3.
Kleman, J., Hättestrand, C., Borgström, I., Stroeven, A., 1997. Fennoscandian palaeoglaciology reconstructed using a glacial geological inversion model. J. Glaciol. 43 (144), 283–299. http://dx.doi.org/10.3198/1997JoG43-144-283-299.
Kleman, J., Hättestrand, C., Clarhäll, A., 1999. Zooming in on frozen-bed patches: scale-dependent controls on Fennoscandian ice sheet basal thermal zonation. Ann. Glaciol. 28 (1), 189–194. http://dx.doi.org/10.3189/172756499781821670.
Kleman, J., Stroeven, A.P., Lundqvist, J., 2008. Patterns of Quaternary ice sheet erosion and deposition in Fennoscandia and a theoretical framework for explanation. Geomorphology 97 (1), 73–90. http://dx.doi.org/10.1016/j.geomorph.2007.02.049.
Knies, J., Vogt, C., Stein, R., 1998. Late Quaternary growth and decay of the Svalbard/Barents Sea ice sheet and paleoceanographic evolution in the adjacent Arctic Ocean. Geo-Marine Lett. 18 (3), 195–202. http://dx.doi.org/10.1007/s003670050068.
Koenigk, T., Mikolajewicz, U., Jungclaus, J.H., Kroll, A., 2009. Sea ice in the Barents Sea: seasonal to interannual variability and climate feedbacks in a global coupled model. Clim. Dyn. 32 (7–8), 1119–1138. http://dx.doi.org/10.1007/s00382-008-0450-2.
Kuchar, J., Milne, G., Hubbard, A., Patton, H., Bradley, S., Shennan, I., Edwards, R., 2012. Evaluation of a numerical model of the British-Irish ice sheet using relative sea-level data: implications for the interpretation of trimline observations. J. Quat. Sci. 27 (6), 597–605. http://dx.doi.org/10.1002/jqs.2552.
Kvasov, D.D., 1978. The Barents ice sheet as a relay regulator of glacial-interglacial alternation. Quat. Res. 9 (3), 288–299. http://dx.doi.org/10.1016/0033-5894(78)90034-0.
Kvenvolden, K.A., 1993. Gas hydrates—geological perspective and global change. Rev. Geophys. 31 (2), 173. http://dx.doi.org/10.1029/93RG00268.
Laberg, J.S., Vorren, T.O., 1995. Late Weichselian submarine debris flow deposits on the Bear Island Trough Mouth Fan. Mar. Geol. 127 (1–4), 45–72. http://dx.doi.org/10.1016/0025-3227(95)00055-4.
Lal, D., 1991. Cosmic ray labeling of erosion surfaces: *in situ* nuclide production rates and erosion models. Earth Planet. Sci. Lett. 104 (2), 424–439. http://dx.doi.org/10.1016/0012-821X(91)90220-C. Elsevier.
Lambeck, K., 1993. Glacial rebound of the British Isles-I. preliminary model results. Geophys. J. Int. 115 (3), 941–959. http://dx.doi.org/10.1111/j.1365-246X.1993.tb01503.x.
Landvik, J.Y., Brook, E.J., Gualtieri, L., Linge, H., Raisbeck, G., Salvigsen, O., Yiou, F., 2013. ^{10}Be exposure age constraints on the Late Weichselian ice-sheet geometry and dynamics in inter-ice-stream areas, western Svalbard. Boreas 42 (1), 43–56. http://dx.doi.org/10.1111/j.1502-3885.2012.00282.x.
Larsen, E., Lyså, A., Demidov, I., Funder, S., Houmark-Nielsen, M., Kjær, K.H., Murray, A.S., 1999. Age and extent of the Scandinavian ice sheet in northwest Russia. Boreas 28 (1), 115–132. http://dx.doi.org/10.1111/j.1502-3885.1999.tb00209.x.
Larsen, E., Fredin, O., Jensen, M., Kuznetsov, D., Lysså, A., Subetto, D., 2014. Subglacial sediment, proglacial lake-level and topographic controls on ice extent and lobe geometries during the Last Glacial Maximum in NW Russia. Quat. Sci. Rev. 92, 369–387. http://dx.doi.org/10.1016/j.quascirev.2013.02.018.
Laumann, T., Reeh, N., 1993. Sensitivity to climate-change of the mass-balance of glaciers in southern Norway. J. Glaciol. 39 (133), 656–665. http://dx.doi.org/10.3198/1993JoG39-133-656-665.
Le Meur, E., Huybrechts, P., 1996. A comparison of different ways of dealing with isostasy: examples from modeling the Antarctic ice sheet during the last glacial cycle. Ann. Glaciol. 23, 309–317.
Li, Y., Napieralski, J., Harbor, J., 2008. A revised automated proximity and conformity analysis method to compare predicted and observed spatial boundaries of geologic phenomena. Comput. Geosciences 34 (12), 1806–1814. http://dx.doi.org/10.1016/j.cageo.2008.01.003.
Linge, H., Brook, E.J., Nesje, A., Raisbeck, G.M., Yiou, F., Clark, H., 2006. In situ ^{10}Be exposure ages from southeastern Norway: implications for the geometry of the Weichselian Scandinavian ice sheet. Quat. Sci. Rev. 25 (9–10), 1097–1109. http://dx.doi.org/10.1016/j.quascirev.2005.10.007.
Luckman, A., Benn, D.I., Cottier, F., Bevan, S., Nilsen, F., Inall, M., 2015. Calving rates at tidewater glaciers vary strongly with ocean temperature. Nat. Commun. 6, 8566. http://dx.doi.org/10.1038/ncomms9566.
Mangerud, J., Gosse, J., Matiouchkov, A., Dolvik, T., 2008a. Glaciers in the Polar Urals, Russia, were not much larger during the Last Global Glacial Maximum than today. Quat. Sci. Rev. 27 (9–10), 1047–1057. http://dx.doi.org/10.1016/j.quascirev.2008.01.015.
Mangerud, J., Kaufman, D., Hansen, J., Svendsen, J.I., 2008b. Ice-free conditions in Novaya Zemlya 35 000–30 000 cal years B.P., as indicated by radiocarbon ages and amino acid racemization evidence from marine molluscs. Polar Res. 27 (2), 187–208. http://dx.doi.org/10.3402/polar.v27i2.6176.
Mangerud, J., Gulliksen, S., Larsen, E., 2010. ^{14}C-dated fluctuations of the western flank of the Scandinavian Ice Sheet 45-25 kyr BP compared with Bølling-Younger Dryas fluctuations and Dansgaard-Oeschger events in Greenland. Boreas 39 (2), 328–342. http://dx.doi.org/10.1111/j.1502-3885.2009.00127.x.
Marshall, S.J., Björnsson, H., Flowers, G.E., Clarke, G.K.C., 2005. Simulation of Vatnajökull ice cap dynamics. J. Geophys. Res. Earth Surf. 110 (F3), F03009. http://dx.doi.org/10.1029/2004JF000262.
Marsiat, I., Valdes, P.J., 2001. Sensitivity of the Northern Hemisphere climate of the Last Glacial Maximum to sea surface temperatures. Clim. Dyn. 17 (2–3), 233–248. http://dx.doi.org/10.1007/s003820000108.
Merritt, J.W., Connell, E.R., Hall, A.M., 2016. Middle to Late Devensian glaciation of north-east Scotland: implications for the north-eastern quadrant of the last British-Irish ice sheet. J. Quat. Sci. http://dx.doi.org/10.1002/jqs.2878.
Milne, G.A., Davis, J.L., Mitrovica, J.X., Scherneck, H.G., Johansson, J.M., Vermeer, M., Koivula, H., 2001. Space-geodetic constraints on glacial isostatic adjustment in Fennoscandia. Science 291 (5512), 2381–2385. http://dx.doi.org/10.1126/science.1057022.
Möller, P., Anjar, J., Murray, A.S., 2013. An OSL-dated sediment sequence at Idre, west-central Sweden, indicates ice-free conditions in MIS 3. Boreas 42 (1), 25–42. http://dx.doi.org/10.1111/j.1502-3885.2012.00284.x.
Möller, P., Alexanderson, H., Funder, S., Hjort, C., 2015. The Taimyr Peninsula and the Severnaya Zemlya archipelago, Arctic Russia: a synthesis of glacial history and palaeo-environmental change during the Last Glacial cycle (MIS 5e–2). Quat. Sci. Rev. 107, 149–181. http://dx.doi.org/10.1016/j.quascirev.2014.10.018.
Morlighem, M., Bondzio, J., Seroussi, H., Rignot, E., Larour, E., Humbert, A., Rebuffi, S., 2016. Modeling of Store Gletscher's calving dynamics, West Greenland, in response to ocean thermal forcing. Geophys. Res. Lett. 43 (6), 2659–2666. http://dx.doi.org/10.1002/2016GL067695.
Mörner, N.-A., 1990. Glacial isostasy and long-term crustal movements in Fennoscandia with respect to lithospheric and asthenospheric processes and properties. Tectonophysics 176 (1–2), 13–24. http://dx.doi.org/10.1016/0040-1951(90)90256-8.
Müller, J., Stein, R., 2014. High-resolution record of late glacial and deglacial sea ice changes in Fram Strait corroborates ice–ocean interactions during abrupt climate shifts. Earth Planet. Sci. Lett. 403, 446–455. http://dx.doi.org/10.1016/j.epsl.2014.07.016.
Müller, J., Massé, G., Stein, R., Belt, S.T., 2009. Variability of sea-ice conditions in the Fram Strait over the past 30,000 years. Nat. Geosci. 2 (11), 772–776. http://dx.doi.org/10.1038/ngeo665.
Napieralski, J., Li, Y., Harbor, J., 2006. Comparing predicted and observed spatial boundaries of geologic phenomena: Automated Proximity and Conformity Analysis applied to ice sheet reconstructions. Comput. Geosciences 32 (1), 124–134. http://dx.doi.org/10.1016/j.cageo.2005.05.011.
Napieralski, J., Hubbard, A., Li, Y., Harbor, J., Stroeven, A.P., Kleman, J., Alm, G., Jansson, K.N., 2007. Towards a GIS assessment of numerical ice-sheet model performance using geomorphological data. J. Glaciol. 53 (180), 71–83. http://dx.doi.org/10.3189/172756507781833884.
Oerlemans, J., 1984. Numerical experiments on glacial erosion. Z. für Gletscherkd. Glazialgeol. 20, 107–126.
Ohmura, A., Calanca, P., Wild, M., Anklin, M., 1999. Precipitation, accumulation and mass balance of the Greenland ice sheet. Z. fur Gletscherkd. Glazialgeol. 31 (1), 1–20.
Ottesen, D., Dowdeswell, J.A., Rise, L., 2005. Submarine landforms and the reconstruction of fast-flowing ice streams within a large Quaternary ice sheet: the 2500-km-long Norwegian-Svalbard margin (57°–80°N). Geol. Soc. Am. Bull. 117

(7), 1033. http://dx.doi.org/10.1130/B25577.1.
Patton, H., Hubbard, A., Glasser, N.F., Bradwell, T., Golledge, N.R., 2013. The last Welsh Ice Cap: Part 1-Modelling its evolution, sensitivity and associated climate. Boreas 42 (3), 471–490. http://dx.doi.org/10.1111/j.1502-3885.2012.00300.x.
Patton, H., Andreassen, K., Bjarnadóttir, L.R., Dowdeswell, J.A., Winsborrow, M.C.M., Noormets, R., Polyak, L., Auriac, A., Hubbard, A., 2015. Geophysical constraints on the dynamics and retreat of the Barents Sea Ice Sheet as a palaeo-benchmark for models of marine ice-sheet deglaciation. Rev. Geophys. 53 (4), 1051–1098. http://dx.doi.org/10.1002/2015RG000495.
Pattyn, F., Perichon, L., Aschwanden, A., Breuer, B., de Smedt, B., Gagliardini, O., Gudmundsson, G.H., Hindmarsh, R.C.A., Hubbard, A., Johnson, J.V., Kleiner, T., Konovalov, Y., Martin, C., Payne, A.J., Pollard, D., Price, S., Rückamp, M., Saito, F., Souček, O., Sugiyama, S., Zwinger, T., 2008. Benchmark experiments for higher-order and full-Stokes ice sheet models (ISMIP–HOM). Cryosphere 2 (2), 95–108. http://dx.doi.org/10.5194/tc-2-95-2008.
Paus, A., Velle, G., Berge, J., 2011. The Lateglacial and early Holocene vegetation and environment in the Dovre mountains, central Norway, as signalled in two Lateglacial nunatak lakes. Quat. Sci. Rev. 30 (13–14), 1780–1796. http://dx.doi.org/10.1016/j.quascirev.2011.04.010.
Payne, A.J., 1999. A thermomechanical model of ice flow in West Antarctica. Clim. Dyn. 15 (2), 115–125. http://dx.doi.org/10.1007/s003820050271.
Peltier, W.R., 2004. Global glacial isostasy and the surface of the ice-age Earth: the ICE-5G (VM2) Model and GRACE. Annu. Rev. Earth Planet. Sci. 32 (1), 111–149. http://dx.doi.org/10.1146/annurev.earth.32.082503.144359.
Peltier, W.R., Fairbanks, R.G., 2006. Global glacial ice volume and Last Glacial Maximum duration from an extended Barbados sea level record. Quat. Sci. Rev. 25 (23–24), 3322–3337. http://dx.doi.org/10.1016/j.quascirev.2006.04.010.
Peltier, W.R., Argus, D.F., Drummond, R., 2015. Space geodesy constrains ice age terminal deglaciation: the global ICE-6G_C (VM5a) model. J. Geophys. Res. Solid Earth 120 (1), 450–487. http://dx.doi.org/10.1002/2014JB011176.
Peters, J.L., Benetti, S., Dunlop, P., Ó Cofaigh, C., 2015. Maximum extent and dynamic behaviour of the last British–Irish Ice Sheet west of Ireland. Quat. Sci. Rev. 128, 48–68. http://dx.doi.org/10.1016/j.quascirev.2015.09.015.
Peyaud, V., Ritz, C., Krinner, G., 2007. Modelling the Early Weichselian Eurasian Ice Sheets: role of ice shelves and influence of ice-dammed lakes. Clim. Past 3, 375–386. http://dx.doi.org/10.5194/cp-3-375-2007.
Pollack, H.N., Hurter, S.J., Johnson, J.R., 1993. Heat flow from the Earth's interior: analysis of the global data set. Rev. Geophys. 31 (3), 267. http://dx.doi.org/10.1029/93RG01249.
Pollard, D., DeConto, R.M., 2007. A coupled ice-sheet/ice-shelf/sediment model applied to a marine-margin flowline: forced and unforced variations. In: Hambrey, M.J., Christoffersen, P., Glasser, N.F., Hubbard, B. (Eds.), Glacial Sedimentary Processes and Products. Blackwell Publishing Ltd, Oxford.
Polyak, L., Forman, S.L., Herlihy, F.A., Ivanov, G., Krinitsky, P., 1997. Late Weichselian deglacial history of the Svyataya (Saint) Anna Trough, northern Kara Sea, Arctic Russia. Mar. Geol. 143 (1–4), 169–188. http://dx.doi.org/10.1016/S0025-3227(97)00096-0.
Polyak, L., Gataullin, V., Gainanov, V., Gladysh, V., Goremykin, Y., 2002. Kara Sea expedition yields insight into extent of LGM ice sheet. Eos, Trans. Am. Geophys. Union 83 (46), 525. http://dx.doi.org/10.1029/2002EO000361, 529–530.
Polyak, L., Niessen, F., Gataullin, V., Gainanov, V., 2008. The eastern extent of the Barents-Kara ice sheet during the Last Glacial Maximum based on seismic-reflection data from the eastern Kara Sea. Polar Res. 27 (2), 162–174. http://dx.doi.org/10.1111/j.1751-8369.2008.00061.x.
Portnov, A., Vadakkepuliyambatta, S., Mienert, J., Hubbard, A., 2016. Ice-sheet-driven methane storage and release in the Arctic. Nat. Commun. 7, 10314. http://dx.doi.org/10.1038/ncomms10314.
Praeg, D., McCarron, S., Dove, D., Ó Cofaigh, C., Scott, G., Monteys, X., Facchin, L., Romeo, R., Coxon, P., 2015. Ice sheet extension to the Celtic Sea shelf edge at the Last Glacial Maximum. Quat. Sci. Rev. 111, 107–112. http://dx.doi.org/10.1016/j.quascirev.2014.12.010.
Rachold, V., Bolshiyanov, D.Y., Grigoriev, M.N., Hubberten, H.-W., Junker, R., Kunitsky, V.V., Merker, F., Overduin, P., Schneider, W., 2007. Nearshore Arctic subsea permafrost in transition. Eos, Trans. Am. Geophys. Union 88 (13), 149–150. http://dx.doi.org/10.1029/2007EO130001.
Rørvik, K.-L., Laberg, J.S., Hald, M., Ravna, E.K., Vorren, T.O., 2010. Behavior of the northwestern part of the Fennoscandian ice sheet during the Last Glacial Maximum – a response to external forcing. Quat. Sci. Rev. 29 (17–18), 2224–2237. http://dx.doi.org/10.1016/j.quascirev.2010.05.022.
Sarala, P., 2006. Ribbed moraine stratigraphy and formation in southern Finnish Lapland. J. Quat. Sci. 21 (4), 387–398. http://dx.doi.org/10.1002/jqs.995.
Scourse, J.D., Haapaniemi, A.I., Colmenero-Hidalgo, E., Peck, V.L., Hall, I.R., Austin, W.E.N., Knutz, P.C., Zahn, R., 2009. Growth, dynamics and deglaciation of the last British–Irish ice sheet: the deep-sea ice-rafted detritus record. Quat. Sci. Rev. 28 (27–28), 3066–3084. http://dx.doi.org/10.1016/j.quascirev.2009.08.009.
Seguinot, J., 2013. Spatial and seasonal effects of temperature variability in a positive degree-day glacier surface mass-balance model. J. Glaciol. 59 (218), 1202–1204. http://dx.doi.org/10.3189/2013JoG13J081.
Sejrup, H.P., Larsen, E., Landvik, J., King, E.L., Haflidason, H., Nesje, A., 2000. Quaternary glaciations in southern Fennoscandia: evidence from southwestern Norway and the northern North Sea region. Quat. Sci. Rev. 19 (7), 667–685. http://dx.doi.org/10.1016/S0277-3791(99)00016-5.
Sejrup, H.P., Hjelstuen, B.O., Dahlgren, K.I.T., Haflidason, H., Kuijpers, A., Nygård, A., Praeg, D., Stoker, M.S., Vorren, T.O., 2005. Pleistocene glacial history of the NW European continental margin. Mar. Petroleum Geol. 22 (9–10), 1111–1129. http://dx.doi.org/10.1016/j.marpetgeo.2004.09.007.
Sejrup, H.P., Nygård, A., Hall, A.M., Haflidason, H., 2009. Middle and Late Weichselian (Devensian) glaciation history of south-western Norway, North Sea and eastern UK. Quat. Sci. Rev. 28 (3–4), 370–380. http://dx.doi.org/10.1016/j.quascirev.2008.10.019.
Sejrup, H.P., Clark, C.D., Hjelstuen, B.O., 2016. Rapid ice sheet retreat triggered by ice stream debuttressing: evidence from the North Sea. Geology 44 (5), 355–358. http://dx.doi.org/10.1130/G37652.1.
Serov, P., Portnov, A., Mienert, J., Semenov, P., Ilatovskaya, P., 2015. Methane release from pingo-like features across the South Kara Sea shelf, an area of thawing offshore permafrost. J. Geophys. Res. Earth Surf. 120 (8), 1515–1529. http://dx.doi.org/10.1002/2015JF003467.
Siegert, M.J., Dowdeswell, J.A., 2004. Numerical reconstructions of the Eurasian Ice Sheet and climate during the Late Weichselian. Quat. Sci. Rev. 23 (11–13), 1273–1283. http://dx.doi.org/10.1016/j.quascirev.2003.12.010.
Siegert, M.J., Marsiat, I., 2001. Numerical reconstructions of LGM climate across the Eurasian Arctic. Quat. Sci. Rev. 20 (15), 1595–1605. http://dx.doi.org/10.1016/S0277-3791(01)00017-8.
Siegert, M.J., Dowdeswell, J.A., Hald, M., Svendsen, J.-I., 2001. Modelling the Eurasian Ice Sheet through a full (Weichselian) glacial cycle. Glob. Planet. Change 31 (1–4), 367–385. http://dx.doi.org/10.1016/S0921-8181(01)00130-8.
Spielhagen, R.F., Baumann, K.-H., Erlenkeuser, H., Nowaczyk, N.R., Nørgaard-Pedersen, N., Vogt, C., Weiel, D., 2004. Arctic Ocean deep-sea record of northern Eurasian ice sheet history. Quat. Sci. Rev. 23 (11–13), 1455–1483. http://dx.doi.org/10.1016/j.quascirev.2003.12.015.
Stein, R., Niessen, F., Dittmers, K., Levitan, M., Schoster, F., Simstich, J., Steinke, T., Stepanets, O.V., 2002. Siberian river run-off and late quaternary glaciation in the southern Kara sea, Arctic Ocean: preliminary results. Polar Res. 21 (2), 315–322. http://dx.doi.org/10.1111/j.1751-8369.2002.tb00086.x.
Stone, J.O., 2000. Air pressure and cosmogenic isotope production. J. Geophys. Res. Solid Earth 105 (B10), 23753–23759. http://dx.doi.org/10.1029/2000JB900181.
Straneo, F., Sutherland, D.A., Holland, D., Gladish, C., Hamilton, G.S., Johnson, H.L., Rignot, E., Xu, Y., Koppes, M., 2012. Characteristics of ocean waters reaching Greenland's glaciers. Ann. Glaciol. 53 (60), 202–210. http://dx.doi.org/10.3189/2012AoG60A059.
Stroeven, A.P., Harbor, J., Fabel, D., Kleman, J., Hättestrand, C., Elmore, D., Fink, D., Fredin, O., 2006. Slow, patchy landscape evolution in northern Sweden despite repeated ice-sheet glaciation. In: Willett, S.D., Hovius, N., Brandon, M.T., Fisher, D.M. (Eds.), GSA Special Paper, 398, Tectonics, Climate and Landscape Evolution. Geological Society of America, pp. 387–396. http://dx.doi.org/10.1130/2006.2398(24).
Stroeven, A.P., Hättestrand, C., Kleman, J., Heyman, J., Fabel, D., Fredin, O., Goodfellow, B.W., Harbor, J.M., Jansen, J.D., Olsen, L., Caffee, M.W., Fink, D., Lundqvist, J., Rosqvist, G.C., Strömberg, B., Jansson, K.N., 2016. Deglaciation of Fennoscandia. Quat. Sci. Rev. 147, 91–121. http://dx.doi.org/10.1016/j.quascirev.2015.09.016.
Svendsen, J.I., Alexanderson, H., Astakhov, V.I., Demidov, I., Dowdeswell, J.A., Funder, S., Gataullin, V., Henriksen, M., Hjort, C., Houmark-Nielsen, M., Hubberten, H.W., Ingólfsson, Ó., Jakobsson, M., Kjær, K.H., Larsen, E., Lokrantz, H., Lunkka, J.P., Lyså, A., Mangerud, J., Matiouchkov, A., Murray, A., Möller, P., Niessen, F., Nikolskaya, O., Polyak, L., Saarnisto, M., Siegert, C., Siegert, M.J., Spielhagen, R.F., Stein, R., 2004. Late Quaternary ice sheet history of northern Eurasia. Quat. Sci. Rev. 23 (11–13), 1229–1271. http://dx.doi.org/10.1016/j.quascirev.2003.12.008.
Svendsen, J.I., Briner, J.P., Mangerud, J., Young, N.E., 2015. Early break-up of the Norwegian Channel ice stream during the Last Glacial Maximum. Quat. Sci. Rev. 107, 231–242. http://dx.doi.org/10.1016/j.quascirev.2014.11.001.
Tarasov, L., Peltier, W.R., 2000. Laurentide ice sheet aspect ratio in models based on Glen's flow law. Ann. Glaciol. 30 (1), 177–186. http://dx.doi.org/10.3189/172756400781820804.
Thomas, E.R., Mulvaney, R., Wolff, E.W., 2008. A change in seasonality in Greenland during a Dansgaard–Oeschger warming. Ann. Glaciol. 48 (1), 19–24. http://dx.doi.org/10.3189/172756408784700590.
Todd, J., Christoffersen, P., 2014. Are seasonal calving dynamics forced by buttressing from ice mélange or undercutting by melting? Outcomes from full-Stokes simulations of Store Glacier, West Greenland. Cryosphere 8 (6), 2353–2365. http://dx.doi.org/10.5194/tc-8-2353-2014.
Ukkonen, P., Arppe, L., Houmark-Nielsen, M., Kjær, K.H., Karhu, J.A., 2007. MIS 3 mammoth remains from Sweden—implications for faunal history, palaeoclimate and glaciation chronology. Quat. Sci. Rev. 26 (25–28), 3081–3098. http://dx.doi.org/10.1016/j.quascirev.2007.06.021.
van den Berg, J., van de Wal, R., Oerlemans, H., 2008. A mass balance model for the Eurasian Ice Sheet for the last 120,000 years. Glob. Planet. Change 61 (3–4), 194–208. http://dx.doi.org/10.1016/j.gloplacha.2007.08.015.
van der Veen, C.J., 1998. Fracture mechanics approach to penetration of surface crevasses on glaciers. Cold Regions Sci. Technol. 27 (1), 31–47. http://dx.doi.org/10.1016/S0165-232X(97)00022-0.
van der Veen, C.J., 1999. Fundamentals of Glacier Dynamics. A.A. Balkema, Rotterdam.
van der Veen, C.J., 2002. Polar ice sheets and global sea level: how well can we predict the future? Glob. Planet. Change 32 (2–3), 165–194. http://dx.doi.org/10.1016/S0921-8181(01)00140-0.
Vorren, T.O., Laberg, J.S., 1997. Trough mouth fans — palaeoclimate and ice-sheet

monitors. Quat. Sci. Rev. 16 (8), 865–881. http://dx.doi.org/10.1016/S0277-3791(97)00003-6.
Waelbroeck, C., Labeyrie, L., Michel, E., Duplessy, J.C., McManus, J.F., Lambeck, K., Balbon, E., Labracherie, M., 2002. Sea-level and deep water temperature changes derived from benthic foraminifera isotopic records. Quat. Sci. Rev. 21 (1–3), 295–305. http://dx.doi.org/10.1016/S0277-3791(01)00101-9.
Weertman, J., 1964. The theory of glacier sliding. J. Glaciol. 5, 287–303.
Whittington, G., Hall, A.M., 2002. The Tolsta Interstadial, Scotland: correlation with D–O cycles GI-8 to GI-5? Quat. Sci. Rev. 21 (8–9), 901–915. http://dx.doi.org/10.1016/S0277-3791(01)00068-3.
Wilch, E., Hughes, T.J., 2000. Calculating basal thermal zones beneath the Antarctic ice sheet. J. Glaciol. 46 (153), 297–310. http://dx.doi.org/10.3189/172756500781832927.
Winsborrow, M.C.M., Andreassen, K., Corner, G.D., Laberg, J.S., 2010. Deglaciation of a marine-based ice sheet: Late Weichselian palaeo-ice dynamics and retreat in the southern Barents Sea reconstructed from onshore and offshore glacial geomorphology. Quat. Sci. Rev. 29 (3–4), 424–442. http://dx.doi.org/10.1016/j.quascirev.2009.10.001.
Winsborrow, M., Andreassen, K., Hubbard, A., Plaza-Faverola, A., Gudlaugsson, E., Patton, H., 2016. Regulation of ice stream flow through subglacial formation of gas hydrates. Nat. Geosci. 9 (5), 370–374. http://dx.doi.org/10.1038/ngeo2696.
Wohlfarth, B., Näslund, J.-O., 2010. Fennoscandian ice sheet in MIS 3-Introduction. Boreas 39 (2), 325–327. http://dx.doi.org/10.1111/j.1502-3885.2009.00151.x.